

---

## Strong geochemical anomalies following active submarine eruption offshore Mayotte

Mastin Manon <sup>1, \*</sup>, Cathalot Cécile <sup>1</sup>, Fandino Olivia <sup>1</sup>, Giunta Thomas <sup>1</sup>, Donval Jean-Pierre <sup>1</sup>, Guyader Vivien <sup>1</sup>, Germain Yoan <sup>1</sup>, Scalabrin Carla <sup>1</sup>, Dehez Sébastien <sup>2</sup>, Jouenne Stéphane <sup>2</sup>, Gaucher Eric C. <sup>3</sup>, Rouxel Olivier <sup>1</sup>, Rinnert Emmanuel <sup>1</sup>

<sup>1</sup> Geo-Ocean UMR 6538 CNRS - Ifremer - UBO - UBS, F-29280 Plouzané, France

<sup>2</sup> TotalEnergies, CSTJF EB 437, Avenue Larribau, F-64018 Pau Cedex, France

<sup>3</sup> Lavoisier H2 Geoconsult, FR-74400 Chamonix, France

\* Corresponding author : Manon Mastin, email address : [manon.mastin@ifremer.fr](mailto:manon.mastin@ifremer.fr)

---

### Abstract :

Submarine volcanic activity releases large amounts of gases and metals in the water column, affecting biogeochemical cycles and ecosystems at a regional and local scale. In 2018, Fani Maoré submarine volcano erupted 50 km offshore Mayotte Island (Comoros Archipelago, Indian Ocean). Active eruptive plumes were observed in May 2019 at and around the summit with acoustic plumes rising 2 km into the water column coupled to strong geochemical anomalies. Between May 2019 and October 2020, three research cruises monitored the eruptive activity. Here, we report spatial and temporal variability of water column chemistry above the volcano, focusing on dissolved gases, trace metal concentrations, and physico-chemical parameters. In May 2019, concentrations above 800 nM in CH<sub>4</sub> and H<sub>2</sub> were measured throughout the water column, with Total Dissolvable Mn and Total Dissolvable Fe concentrations above 500 nM, and CO<sub>2</sub> values of 265 μM. Strong water column acidification was measured (0.6 pH unit) compared to the regional background. From May 2019 to October 2020, we observed a general decrease in gas concentrations, and an evolution of the TDMn/TDFe ratios similar to previously reported values in other submarine volcanic contexts, and consistent with a decrease of the eruptive activity at the volcano. In October 2020, a rebound of high H<sub>2</sub> concentrations resulted from new lava flows, which were identified by seafloor observation using deep-towed camera, 5 km further than the volcano summit. During 2 years timespan of our observations (2019–2020), He, CO<sub>2</sub> and CH<sub>4</sub> concentrations correlate highlighting a magmatic origin of dissolved gases. δ<sup>13</sup>C-CH<sub>4</sub> values of -34‰ vs. vPDB might suggest magma/sediments interaction during the magma ascent, and potential thermal cracking of organic matter, although abiotic methane generation cannot be ruled out given the volcanic context. Weak correlations between H<sub>2</sub> and excess of <sup>3</sup>He suggest complex processes of H<sub>2</sub> from magmatic degassing, lava/seawater interaction, and oxidation processes in the water column. Strong and correlated Fe, Mn and Si water column anomalies are also consistent with fluid-rock reactions induced by acidic fluids rich in magmatic volatiles. Water column acidification appears to be associated with the release of CO<sub>2</sub>-rich fluids. A year after the main eruptive event, the system seems to be back to steady-state highlighting the buffer capacity and resilience of the seawater column environment.

---

## Highlights

- ▶ Massive gases released in the water column during the eruption.
- ▶ Emitted gases respond in an uncoupled way due to original settings of the volcano.
- ▶ Strong water column acidification due to the release of CO<sub>2</sub>-rich fluids.
- ▶ Water column enrichments in iron and manganese by fluid-rock interactions.
- ▶ Helium isotope signatures show evidence of a change in the magma path.

**Keywords** : Mayotte, submarine eruption, volcano, geochemistry, dissolved gases

# 1 INTRODUCTION

Submarine volcanism represents about 85% of the global Earth volcanism (White et al., 2015). It is responsible for the transfer of chemicals from the crust to the water column, including volatile elements or reduced transition metals, and is also the main mechanism responsible for deep stored carbon release to the surface (Baker et al., 2012; Rubin et al., 2012). Water column geochemical signature of submarine eruptions are quite different from one site to another but generally exhibit increases in magmatic volatile gases ( $^3\text{He}$ ,  $\text{CO}_2$ ), enrichments in  $\text{H}_2$  and  $\text{CH}_4$ , decreases in pH by the addition of  $\text{CO}_2$ ,  $\text{SO}_2$  and mineral acidity ( $\text{H}^+$ ), and discharges of reduced species including  $\text{H}_2\text{S}$  (Baumberger et al., 2014; Buck et al., 2018; Resing et al., 2009; Resing et al., 2007). Each of these compounds are valuable tracers for submarine eruptions and hydrothermal circulation: combining them bring insights of their origin and generation mechanisms involved.

Studies on submarine eruptions started in the 1980's, but deep-sea eruptions are very difficult to detect and observe due to their shortness (Baker et al., 2012; Rubin et al., 2012). They have mostly been sampled after the end of the eruption, often capturing the hydrothermal activity state instead of the eruptive state (Rubin et al., 2012). Before the Mayotte submarine eruption, only three active submarine eruptions have been observed: NW Rota-1 (an explosive shallow eruption – at ~500 m deep – in the Mariana arc (Chadwick et al., 2008)), West-Mata (a deeper

explosive eruption – at ~1200 m deep – in the Lau basin (Embley et al., 2014; Resing et al., 2011)), and event plumes at the NE Lau Spreading Center eruption (rising from summits between 1600 and 1300 m deep, Baker et al (2011)). The Mayotte submarine eruption and the significant scientist mobilization that followed offer well-defined temporal and spatial constraints on the birth of a volcanic edifice, and constitutes therefore a great opportunity to study the origin and processes responsible for gas release, their impact in the water column and the carbonate system response.

After a few thousand years of aseismicity, (Zinke et al., 2003a), in May 2018, Mayotte Island started to experience a major seismic crisis. This phenomenon was associated with the birth of a volcano edifice 50 km East offshore Mayotte, with characteristics that make it the largest active eruption ever documented since the Laki eruption in 1783 (Thordarson and Self, 1993). Indeed, this volcano stands 820 m above the seafloor, with a magma released estimated to be about 6.5 km<sup>3</sup>, inducing strong geochemical anomalies through the water column (Cesca et al., 2020; Feuillet et al., 2021; Leroirne et al., 2020). We present here for the first time a comprehensive survey of gas chemistry (H<sub>2</sub>, CO<sub>2</sub>, CH<sub>4</sub> and He) in the water column and its evolution from the birth of the volcano (i.e. eruptive state) to the initiation of hydrothermal activity, covering a time period of about 30 months, from May 2018 to October 2020. We aim to discuss the concomitant evolution of water column chemistry over the course of the eruption and discuss the geochemical mechanisms involved. For instance, the isotopic composition of He provides a valuable and reliable indicator of its own origin but can be decoupled from the more reactive gases (Giggenbach et al., 1993). Indeed, the presence of primordial <sup>3</sup>He within the water column indicates input of magmatic gases from the mantle (Craig and Lupton, 1981), whereas radiogenic <sup>4</sup>He indicates gas inputs originating from the crust (Barry et al., 2020). Aside from hydrothermal reactions (e.g. serpentinization), generation of H<sub>2</sub> occurs during lava and seawater interactions, generally associated with gas-

rich eruptions (Sansone et al., 1991). In submarine volcanic systems,  $H_2$  is therefore the typical tracer for ongoing eruption, with a short residence time as it is rapidly consumed by microorganisms and chemical oxidation over hourly or daily timescales (Baumberger et al., 2020; Baumberger et al., 2014). On another hand, methane can be a major component of hydrothermal gases but is usually present in trace amounts in volcanic gases. In natural systems,  $CH_4$  may originate from thermocatalytic decomposition of organic matter, microbial production or from abiotic processes that may involve various chemical reactions (Fiebig et al. (2004) and references therein). In marine hydrothermal systems for instance, methane is thought to be generated abiotically during fluid-rock interactions involving serpentinization reactions and Fischer-Tropsch-type chemical reactions (Giggenbach, 1996; Truche et al., 2020). It is a potent greenhouse gas, 28 times more than  $CO_2$  (Pörtner et al., 2022), with a potential significant effect on past climate change with volcanic basins providing a setting for rapid disruptions in the release of carbon from sedimentary reservoirs (Raynaud et al., 1993; Svensen et al., 2004).

The carbon dioxide is generally the predominant dissolved gases in submarine volcanic fluids, generated through lava outgassing (Craig and Lupton, 1981). Therefore, volcanic activity contributes to local ocean acidification, in particular by the discharge of  $CO_2$ -rich fluids into the seawater column (Resing et al., 2009; Santana-Casiano et al., 2016). Carbon dioxide is an acid gas that reacts with water to produce carbonic acid ( $H_2CO_3$ ) which is dissociated into hydrogenocarbonate ( $HCO_3^-$ ) and carbonate ( $CO_3^{2-}$ ) ions depending on pH and buffer capacity of the solution. When  $CO_2$  is added to a solution, it gives a mixture of these three species that results in an increase of the quantity of total dissolved inorganic carbon (expressed as  $\Sigma CO_2$ ). Those dissolved compounds make up the carbonate system in water. The carbonate system of the ocean is the primary buffer for the acidity of seawater and acts as a governor for the carbon cycle by controlling the partial pressure of  $CO_2$  in the atmosphere, which helps to

regulate the temperature of the planet. The formation rate of the most prevalent authigenic mineral in the environment,  $\text{CaCO}_3$ , is also the major sink for dissolved carbon in the long-term global carbon balance (Emerson and Hedges, 2008). The emission of  $\text{CO}_2$  from submarine volcanoes generates local ocean acidification and a change in the carbonate system equilibrium that could affect biological communities, with especially important consequences for organisms that use calcium carbonate in their structures (Santana-Casiano et al., 2016). This process also favors the photosynthesis (Jansson and Northen, 2010; Suzuki, 1998).

In this study, we present a compilation of geochemical data taken at the Fani Maoré submarine volcano, during the main eruptive event in May 2019 and from two cruises performed in July 2019 and October 2020, leading to monitor the continuous lava flow installation. These data provide valuable information on geochemical mechanisms during the setup of a volcanic edifice and on the impact of an eruptive activity on the water column at a local scale.

## **2 GEOLOGICAL SETTING AND OVERVIEW ON THE ERUPTIVE ACTIVITY OFFSHORE MAYOTTE**

Mayotte Island is located in the Comoros Archipelago, within the Mozambique Channel (Indian Ocean) between the eastern coast of the Mozambique Channel and the northern tip of Madagascar (Figure 1.A). The four islands that compose the Comoros Archipelago are aligned along a NW-SE axis (Tzevahirtzian et al., 2021). Mayotte is the easternmost island of the archipelago, and the eldest with a maximum age of 20 Ma for the onset of subaqueous volcanic activity and 11 Ma for the onset of subaerial volcanic activity (Debeuf, 2004; Michon, 2016; Nougier et al., 1986; Pelleter et al., 2014). The last reported volcanic event occurred 4-6 thousand years ago (ka) at Petite-Terre, east of Mayotte (Zinke et al., 2003b).

The origin of the Comoros volcanism is not yet well understood. Two main hypothesis have been developed to explain its origin: (1) a mantle plume that interacts with the oceanic lithosphere (Emerick and Duncan, 1982); (2) a lithospheric deformation that reactivated transform faults and controlled the magma path (Nougier et al., 1986). Recent works suggest that the volcanism is associated with lithospheric deformation rather than the result of a deep mantle plume (Famin et al., 2020; Lemoine et al., 2020; Michon, 2016; Tzevahirtzian et al., 2021).

On May 10<sup>th</sup>, 2018, the major seismo-volcanic crisis that began on Mayotte Island has sparked the interest of scientists and led to the establishment of the Mayotte volcanological and seismological monitoring network, named REVOSIMA (2021). Over a year, 32 earthquakes of  $M_w \geq 5$  were recorded, including the largest event ever recorded in the Comoros Archipelago on the 15<sup>th</sup> of May 2018 with  $M_w = 5.9$  (Cesca et al., 2020; Feuillet et al., 2021; Lemoine et al., 2020). These earthquakes are distributed into two swarms, one proximal and one distal, whose epicenters are respectively located 5-15 km and about 25 km east of Petite-Terre, at 25-50 km depth (Feuillet et al., 2021; Lavayssière et al., 2022). Very long period seismic events (VLP) were frequently recorded suggesting a fluid migration from active magmatic or hydrothermal processes (Lemoine et al., 2020).

This seismo-volcanic crisis is associated with the birth of a volcanic edifice, the Fani Maoré Seamount, discovered in May 2019 during the MAYOBS1 oceanographic cruise (Feuillet, 2019), that was not present in 2014 during the survey operated by the French Naval Hydrographic and Oceanographic Service (SHOM) (Feuillet et al., 2021) (Figure 1.B and C). The edifice is located 50 km east of Mayotte ( $-12^{\circ}54'37''$ ;  $45^{\circ}42'42''$ ) and rises to 820 m at about 3500 m depth. The ongoing eruption was captured in May 2019 by the ship echo sounder with an exceptional acoustic plume of about 2 km high within the water column

associated with strong geochemical anomalies (Feuillet et al., 2021). Lemoine et al. (2020) and Cesca et al. (2020) proposed that the eruptive activity has been going on from June-July 2018 to May 2019, and was fed by a magma reservoir of 10 to 15 km diameter located at 25 to 35 km depth. Dofal et al. (2021) suggested that this magmatic reservoir developed beneath the interface between the mantle lithosphere and the subplateau.

The eruption was followed, from May 2019 to October 2020, by a chronological lava flow emission (REVOSIMA, Février 2021) associated with four new distant exit points: (1) south of the volcano ( $\sim 0.2 \text{ km}^3$  of lava from May 19<sup>th</sup> to June 17<sup>th</sup> 2019); (2) west of the volcano ( $\sim 0.3 \text{ km}^3$  of lava from June 18<sup>th</sup> to July 30<sup>th</sup> 2019); (3) north of the volcano ( $\sim 0.08 \text{ km}^3$  of lava from July 31<sup>st</sup> to August 20<sup>th</sup> 2019); (4) northwest of the volcano ( $\sim 0.8 \text{ km}^3$  of lava from August 21<sup>st</sup> 2019 to May 11<sup>th</sup> 2020); (5) northwest of the volcano ( $\sim 0.1\text{-}0.2 \text{ km}^3$  of lava from May 11<sup>th</sup> to October 11<sup>th</sup> 2020). From the beginning of the eruptive activity, the volume of erupted magma is estimated to be about  $6.5 \text{ km}^3$  (REVOSIMA, Février 2021). The Fani Maoré acoustic plumes ended in the beginning of June 2019 during MAYOBS2 cruise (Jorry, 2019) and the last recorded lava flow occurred between October 2020 (MAYOBS15, Rinnert et al. (2020)) and January 2021 (MAYOBS17, Thion et al. (2021)).

### 3 MATERIALS AND METHODS

The water column above the volcano was monitored during three oceanographic cruises on board the *R/V Marion Dufresne*. The first cruise, *MAYOBS1*, was conducted in 2019 from May 2<sup>nd</sup> to 22<sup>nd</sup> (Feuillet, 2019); the second, *MAYOBS4*, in 2019 from July 19<sup>th</sup> to August 4<sup>th</sup> (Fouquet and Feuillet, 2019); and the third, *MAYOBS15*, in 2020 from October 1<sup>st</sup> to 27<sup>th</sup> (Rinnert et al., 2020). These *MAYOBS* cruises are part of the REVOSIMA survey program



with the aim of monitoring this seismic and volcanic crisis which affects Mayotte Island (Feuillet et al., 2019).

### 3.1 Sampling sites

Stations for hydrocasts were determined according to the presence of acoustic signals from ship echo sounder surveys (Kongsberg EM122  $1^\circ \times 1^\circ$ ) and to seafloor observations from the submersible interactive camera system (SCAMPI, Ifremer). During the first cruise in May 2019, one hydrocast was performed within the 2000 m-high acoustic plume imaged at the volcano summit (MAY01-HY02), and one other above the northern flank of the volcano (MAY01-HY03) (Figure 1B). In July 2019, three CTD (Conductivity, Temperature, and Depth) casts were carried out, one in the same location as MAY01-HY03 (cast MAY04-HY04) and two at the west of the volcano (MAY04-HY07, MAY04-HY09), above the recent lava flow from June 18<sup>th</sup> to July 30<sup>th</sup> 2019, detected by ship echo sounder. The third cruise focused on the northwest new lava flow from May 11<sup>th</sup> to October 11<sup>th</sup> 2020, with a CTD cast performed above incandescent lava (MAY15-HY08) and very recent lava flow (MAY15-HY06).

CTD casts for background water column evaluation (i.e. remote from volcanic activity) were performed in July 2019 and October 2020, tens of kilometers away from the study site. During MAYOBS4, the background cast was done about 20 km southward from the volcano (MAY04-HY03), whereas during MAYOBS15 the background cast was realized about 100 km northeastward (MAY-HY09).

### 3.2 Sampling methods and analysis

We studied physico-chemical parameters of the water column using a Seabird 911 Plus CTD combined with a Seapoint Turbidity Meter sensor. Turbidity measurements are reported

as Nephelometric Turbidity Unit (NTU). Discrete water samples were collected using a 16-bottles carousel equipped with 8 L Niskin water sampling bottles.

Turbidity signals were homogenized by setting the zero value for all hydrocasts studied. This correction was based on the near-zero signal values encountered around 1500 m depth (i.e. below the euphotic zone and above turbidity anomalies linked to the volcanic activity). The average of 100 turbidity values (acquired at a frequency of 1 Hz, for a CTD rosette ascent velocity of 1 m/s) from 1500 m to deeper was determined and then subtracted to the entire turbidity depth profile.

Samples for noble gases, dissolved gases, metals, pH, alkalinity and silicates analyses were directly taken from the Niskin bottles, as described below. Hydrographic parameters are presented in Supplementary Figures 1 and 2.

### 3.2.1 Helium and Neon

Samples for noble gases analysis were collected immediately after the CTD-rosette was retrieved to conserve the integrity of the dissolved gases. Water was flushed into copper tubing carefully checking for the absence of air bubbles and sealed using special stainless clamps (Sültenfuß, 2015). Quantification of helium and neon isotopes ( $^3\text{He}$ ,  $^4\text{He}$ ,  $^{20}\text{Ne}$ ,  $^{22}\text{Ne}$ ) was performed at the Helis Laboratory (Helium isotopes studies, Bremen, Germany) using a mass spectrometric system composed of a quadrupole mass spectrometer (QMS, Balzers QMG112a<sup>®</sup>) and a sector field mass spectrometer (SMS, MAP 215-50<sup>®</sup>). This method yields a precision of  $\pm 0.4\%$  for  $^3\text{He}/^4\text{He}$  ratios and  $\pm 0.8\%$  for helium and neon concentrations (Sültenfuß et al., 2009).

In this study, we choose to define each component of the measured concentrations of  $^3\text{He}$  and  $^4\text{He}$  (i.e. equilibrium, air contamination and non-atmospheric concentrations). Assuming that

the entire Ne concentration comes from atmospheric air, the corrected He concentration from air contamination and atmospheric air in equilibrium is expressed as  ${}^3\text{He}_{xs}$  and  ${}^4\text{He}_{xs}$ . Considering that the tritiogenic  ${}^3\text{He}$  (i.e. resulting from the radioactive decay of tritium) is negligible in the Indian Ocean offshore Mayotte Island (Jenkins et al., 2019), the  ${}^3\text{He}_{xs}$  and  ${}^4\text{He}_{xs}$  should only corresponds to the supply of mantle and crustal helium. Therefore, the

closure equations for neon and helium are: 
$$\begin{cases} Ne_m = Ne_{eq} + Ne_{air} \\ {}^4\text{He}_m = {}^4\text{He}_{eq} + {}^4\text{He}_{air} + {}^4\text{He}_{xs} \\ {}^3\text{He}_m = {}^3\text{He}_{eq} + {}^3\text{He}_{air} + {}^3\text{He}_{xs} \end{cases}$$

with  $m$  the measured concentration,  $eq$  the equilibrium concentration and  $air$  the concentration for air contamination. Equilibrium and air contamination neon concentrations were defined as  $Ne_{eq} = Ne_{atm} \times \beta_{Ne}$  and  $Ne_{air} = Ne_m - Ne_{eq}$ , and helium isotopes concentrations as  ${}^{3,4}\text{He}_{eq} = {}^{3,4}\text{He}_{atm} \times \beta_{He}$  and  ${}^{3,4}\text{He}_{air} = Ne_{air} \times \frac{{}^{3,4}\text{He}_{atm}}{Ne_{atm}}$ .

We introduce solubility coefficients depending on the temperature and salinity conditions of sampling, which vary respectively from 1.44 to 10.82 °C and from 34.64 to 34.90 psu. Solubility coefficients of Ne and He in seawater ( $\beta_{Ne}$  and  $\beta_{He}$ , respectively) were determined for each sample according to the water temperature (T, in kelvin) and salinity (S, in psu) of the sampling depth, using Weiss (1971) solubility equations:

$$\ln\beta_{He} = -34.6261 + 43.0285\left(\frac{100}{T}\right) + 14.1391\ln\left(\frac{T}{100}\right) + S\left[-0.042340 + 0.022624\left(\frac{T}{100}\right) - 0.0033120\left(\frac{T}{100}\right)^2\right]$$

$$\ln\beta_{Ne} = -39.1971 + 51.8013\left(\frac{100}{T}\right) + 15.7699\ln\left(\frac{T}{100}\right) + S\left[-0.124695 + 0.078374\left(\frac{T}{100}\right) - 0.0127972\left(\frac{T}{100}\right)^2\right]$$

The corrected ratio of helium (Rc/Ra) was determined by only applying the correction from atmospheric air contamination, as the equilibrium value ( $\text{He}_{eq}$ ) is not negligible compare to

$\text{He}_{xs}$ . That means,  $Rc = \frac{{}^3\text{He}_{xs} + {}^3\text{He}_{eq}}{{}^4\text{He}_{xs} + {}^4\text{He}_{eq}}$ .

### 3.2.2 Dissolved gases (CH<sub>4</sub>, CO<sub>2</sub>, H<sub>2</sub>)

Water samples for CH<sub>4</sub> analyses were collected into 125 mL two-valve glass ampoules. During MAYOBS1 and MAYOBS4, samples were poisoned with NaN<sub>3</sub> before onshore analyses, whereas during MAYOBS15, samples were analyzed onboard. Both onshore and onboard analyses were performed using the “purge and trap” method developed by Charlou et al. (1987). Dissolved gases were completely extracted by helium purging and trapped onto activated charcoal at -80°C. The CH<sub>4</sub> was desorbed from the trap by increasing the temperature and was injected into a gas chromatograph (GC) equipped with a flame ionization detector (FID) for quantitative analysis. External calibration was performed using a standard gas of CH<sub>4</sub> at appropriate pressure and constant temperature. This method allows the determination of CH<sub>4</sub> concentrations equivalent to those of open ocean seawater (0.3 nM), with residual standard deviation below 2%.

For onboard CO<sub>2</sub> and H<sub>2</sub> analyses, water samples were carefully collected from the Niskin bottles, without injecting air bubbles, in 240 mL brown glass bottles closed by a screw cap fitted with a PTFE/silicone gas tight septum. Analyses were run by gas chromatography coupled to an helium ionization detector (GC-HID) and using the Headspace method developed by Donval and Guyader (2017) which consists of replacing ~20 mL of the seawater sample by a gaseous phase of pure helium in which dissolved gases equilibrate according to solubility coefficients at equilibrium temperature and to water salinity. External calibration was carried out using a standard gas mixture of H<sub>2</sub>, CO<sub>2</sub> injected through 0.50 mL and 2 mL injection loops at appropriate pressure and constant temperature. The detection limit was 1 nM for hydrogen and 0.1 μM for CO<sub>2</sub> with a residual standard deviation of 3%.

For characteristic samples, the headspace phases were transferred in evacuated 12 mL Labco tubes, completed with helium above the atmospheric pressure, and sent to the Isolab b.v.

laboratory (Stable isotopes and geochemical laboratory services, The Netherlands) for  $^{13}\text{C}$  isotopic composition analysis of  $\text{CH}_4$  and  $\text{CO}_2$ , mentioned hereafter as  $\delta^{13}\text{C}\text{-CH}_4$  and  $\delta^{13}\text{C}\text{CO}_2$ . Carbon isotopes of methane were analyzed with an Agilent 6890N GC (Agilent Technologies, Santa Clara, US) interfaced to a Finigan Delta S IRMS (Thermo Scientific, Bremen, Germany) using a Finigan GC-C II interface. The GC is equipped with a 12 m, 0.32 mm Molsieve column (Agilent) and an injection valve. Samples are calibrated regularly against a calibration standard and results are reported in promille vs. vPDB. The minimum concentration needed to perform the analysis is about 25-50 ppn. Carbon isotopes of  $\text{CO}_2$  were analyzed on an Agilent 7890A GC (Agilent Technologies, Santa Clara, US) interfaced to a MAT 253 IRMS (Thermo Scientific, Bremen, Germany) using a GC-Isolink or a Finigan GC-C III interface. The GC is equipped with a 25 m, 0.32 mm Porabond-Q column (Agilent) and an injection valve. Cold trapping is used to pre-concentrate the sample when necessary. Samples are run at least 3 times after which the average of the results is calculated. The system is calibrated at least once a day using an in house natural gas standard and results are reported in promille vs. vPDB. The minimum concentrations needed to perform the analysis depends on sample composition.

### 3.2.3 Total dissolvable iron and manganese (TDFe and TDMn)

Sampling for analysis of total dissolvable iron and manganese, respectively TDFe and TDMn, was carried out in 30 mL low density polyethylene bottles (LDPE, Nalgene<sup>®</sup>) previously washed with 10%<sub>v/v</sub> hydrochloric acid (HCl 37%, Analytical Grade, Merck) then rinsed with ultrapure water (Milli-Q Millipore element system). All raw samples for metal analysis were acidified to 0.025 mol/L hydrochloric acid (ultrapur<sup>®</sup> grade) within 6 hours of sampling. Quantification of TDFe and TDMn was carried out in laboratory at the Pôle Spectrométrie Océan (PSO, Ifremer, Brest, France), using HR-ICP-MS (High Resolution

Inductively Coupled Plasma Mass Spectrometry; Element XR, ThermoFisher Scientific). Samples were spiked with Indium (In) at 2 ppb and diluted by a factor of 100 with 0.28 mol/L distilled nitric acid. This method allows the quantification of metal concentrations in seawater, with detection limits at sub-micromolar order (about 10 nmol/L for Mn and 100 nmol/L for Fe) and residual standard deviation of 3% for TDMn and 2% for TDFe.

### 3.2.4 pH, Total CO<sub>2</sub>, Total Alkalinity, Silicates

Sampling for the study of pH, total alkalinity ( $A_T$ ) and total CO<sub>2</sub> ( $\Sigma\text{CO}_2$ ) was carried out in 30 mL polyethylene bottles (LDPE, Nalgene<sup>®</sup>) previously rinsed with ultrapure water (Milli-Q Millipore element system) and dried. Samples were analyzed onboard for titration of dissolved alkaline species with hydrochloric acid solution (0.01 mol/L HCl Titrinorm) using a titrimeter (Titrino 848, Metrohm<sup>®</sup>) combined with a pH electrode (Metrohm<sup>®</sup>). Total alkalinity and  $\Sigma\text{CO}_2$  were determined from titration equivalence volumes. Residual standard deviations were of 1.04% for pH measurements, and below 2% for DIC and  $A_T$  measurements.

Samples for the quantification of silicates (SiO<sub>2</sub>) were taken in 60 mL polyethylene bottles previously rinsed with ultrapure water (Milli-Q Millipore element system) and dried. Analyses were done onboard during MAYOBS1 and MAYOBS4 cruises, and onshore during MAYOBS15 cruise, by a segmented continuous flow analysis technique using an autoanalyzer (SEAL AutoAnalyzer 3 HR, SEAL Analytical<sup>®</sup>) based on the spectrophotometry detection (Aminot and K erouel, 2007). Residual standard deviation are below 0.2%.

### 3.3 Combined data for background evaluation

Background composition was evaluated by combining data from background hydrocasts performed both during MAYOBS4 (MAY04-HY03) and MAYOBS15 (MAY15-HY09) (Figure 1). We defined the background as an envelope that integrates the variations of water masses and their movements through the seasons. The background reference for turbidity was determined by first combining the turbidity data from both hydrocasts recorded at 1Hz by the CTD. Then averaging over 40 values so that the standard deviation for depth did not exceed 10 m and that a signal frequency of 1/40Hz was obtained. For the chemical parameters studied, the background reference was determined by first combining the two background hydrocasts and then averaging the data over a close depth range. Same depth ranges were used for all parameters. The envelopes were defined by the standard deviations resulting from the combination of the two profiles. (See Supplementary Figure 3).

## **4 RESULTS**

### **4.1 Seafloor observations**

#### **4.1.1 Identification of various lava flows**

Hydrocast sampling was concomitant to lava flow emplacement occurring throughout the volcanic structure. To understand if geochemical anomalies in the water column could be attributed to active or recent lava flows at the bottom, it is important to evaluate the nature of the volcanic seafloor (Table 1). The hydrocast on the northern flank in July 2019 (MAY04-HY04) was performed above an already emplaced lava flow, covered by a fine sediment deposit, with evidence for incipient fluid shimmering, identified during the SCAMPI exploration (Table 1). At the western lava flow, where casts MAY04-HY07 and MAY04-HY09 were performed in July 2019, SCAMPI images show a more recent lava flow with yellowish staining and thin mats of probably microbial origin (Table 1). In October 2020, the northeast lava flow captured at the hydrocast MAY15-HY06 was a very glossy black lava

(Table 1). Combining this visual aspect with bathymetric surveys gives evidence of the very recent nature of these lava flows. At the MAY15-HY08 cast, an active lava flow was identified by incandescent lava observation (Table 1).

#### 4.1.2 Strong turbidity layer

Monitoring of the turbidity (Figure 2) shows a signal evolution from the regional background during the ongoing eruption and the lava flow installation. Outside the zone of influence of the volcano (i.e. background hydrocasts), turbidity does not exceed 0.06 NTU. Below 2000 m deep, maximum turbidity remains lower than 0.02 NTU. In May 2019, during the ongoing eruption, the turbidity at the volcano summit features maxima up to 0.8 NTU. However, these levels were not as significant compared to the turbidity values recorded at the northern flank of the volcano, with a maximum of 1.4 NTU between 2500 and 3000 m depth, reaching the saturation value of the sensor ( $> 4.9$  NTU) over the last 200 m above seafloor. Two months later, in July 2019, at the same location in the northern flank, turbidity ranged from 0.3 to 1.6 NTU between 2000 m and the seafloor. Casts performed at the same time above the recent western lava flow shows the same turbidity pattern, with maximum turbidity zone starting at 2250 m deep. October 2020 monitoring highlight weaker turbidity signal measured above the new lava flow, with anomalies from 2500 m and only up to 0.6 NTU (Figure 2).

## 4.2 Concentration of gases within the water column

### 4.2.1 Helium measurements

From July 2019 to October 2020,  $^3\text{He}_{\text{xs}}$  measurements for depths below 2000 m remain well distinct from the background value ( $\sim 1.5$  fmol/L) (Figure 3; Table 2). The highest  $^3\text{He}_{\text{xs}}$  concentration of 15.4 fmol/L was measured in July above the western lava flow (cast



MAY04-HY07), at 2924 m depth. Seawater samples taken during the same cruise above the northern flank of the edifice (cast MAY04-HY04) show lower  ${}^3\text{He}_{\text{xs}}$  values of 11.3 fmol/L that were still higher than samples from October 2020 taken above the northwest lava flow (casts MAY15-HY06 and MAY15-HY08). These two last CTD casts exhibit similar profiles with maximum  ${}^3\text{He}_{\text{xs}}$  values around 8 fmol/L and 2900 m depth. TDMn concentrations are well correlated with  ${}^3\text{He}_{\text{xs}}$  ( $\text{TDMn} = 8.97 \times 10^{-6} {}^3\text{He}_{\text{xs}}$ ,  $r^2=0.95$ ), while  $\text{CH}_4$  concentrations show weaker correlation with  ${}^3\text{He}_{\text{x}}$  ( $\text{CH}_4 = 20.3 \times 10^{-6} {}^3\text{He}_{\text{xs}}$ ,  $r^2=0.78$ ).  $\text{CO}_2$  concentrations do not show any significant correlation with other gas concentration. (see Supplementary Figure 04).

#### 4.2.2 Concentration of gases above the volcano edifice

During the May 2019 eruption, extremely high  $\text{H}_2$  concentrations, up to 6000 nmol/L, were measured at the volcano summit (cast MAY01-HY02), inside the acoustic plume (Figure 4; Table 3). Samples from the northern flank exhibit lower, but still strong  $\text{H}_2$  concentrations up to 600 nmol/L. In both cases, maxima concentrations are located at remarkably shallow depths within the water column whereas strong  $\text{CO}_2$  and  $\text{CH}_4$  anomalies are found deeper, near the seafloor, with maximum concentrations of 265  $\mu\text{mol/L}$  and 830 nmol/L, respectively. The same cast above the northern flank was also investigated in July 2019 (cast MAY04-HY04) where no eruptive activity was identified. Concentrations of  $\text{H}_2$  and  $\text{CO}_2$  remain at background level whereas  $\text{CH}_4$  anomalies were measured up to 180 nmol/L at depth 2250 m and below 2500 m.

#### 4.2.3 Concentration of gases above new lava flow emplacements

Strong levels of  $\text{H}_2$  were measured above the active lava flow in October 2020 (cast MAY15-HY08), with concentrations up to 650 nmol/L, between 2700 and 3260 m depth (Figure 5; Table 3). Lower  $\text{H}_2$  concentrations, up to 40 nmol/L and near the seafloor, were

found above the recent western lava flow in July 2019 (casts MAY04-HY07 and MAY04-HY09) and the very recent western lava flow from October 2020 (cast MAY15-HY06).

The maxima concentrations in CO<sub>2</sub>, from 95 to 106 µmol/L, were measured in July 2019 above the recent western lava flow (casts MAY04-HY07 and MAY04-HY09). Seawater samples from the very recent northwest lava flow site (cast MAY15-HY06) exhibit lower maximum concentrations, up to 70 µmol/L, while concentrations levels above the active northwest lava flow (cast MAY15-HY08) remains within the background envelope.

Methane concentrations are at their highest level of 780 nmol/L, above the recent western lava flow (casts MAY04-HY07 and MAY04-HY09), with an anomaly that seems to increase progressively as it goes deeper from 2500 to 3200 m below sea level. Lower anomalies, up to 280 nmol/L, were measured in October 2020 above the actively forming lava flow (casts MAY15-HY06 and MAY15-HY08).

### 4.3 Carbon isotope composition

Carbon isotope ratios of CH<sub>4</sub> and CO<sub>2</sub> throughout the water column (referred as  $\delta^{13}\text{C-CH}_4$  and  $\delta^{13}\text{C-CO}_2$  versus VPDB, respectively) display limited variability through time (Table 4). Mean  $\delta^{13}\text{C-CH}_4$  is  $-34.4 \pm 0.6$  ‰ (2.s.d, n = 2), while  $\delta^{13}\text{C-CO}_2$  is  $-1.0 \pm 0.4$  ‰ (2.s.d, n = 6). In this study, we will not use the signature of  $\delta^{13}\text{C-CO}_2$  for data interpretation because, in our water column samples, the CO<sub>2</sub> emitted from the eruption is strongly diluted within the surrounding seawater where the CO<sub>2</sub> is about 30-40 µmol/L. As we do not have endmember values, the signature of the emitted CO<sub>2</sub> is hardly definable. We consider that  $\delta^{13}\text{C-CO}_2$  values result from the mixing between a magmatic component ( $-8$  ‰  $< \delta^{13}\text{C-CO}_2 < -4$  ‰; Sano and Marty (1995)), a marine limestone component (0 ‰; Sano and Marty (1995)), the remineralisation of the organic matter (mean  $\delta^{13}\text{C-CO}_2$  of the marine organic matter is about-

20 ‰; Degens et al. (1968)), and the Indian Ocean seawater composition ( $0.1 ‰ < \delta^{13}\text{C}-\text{CO}_2 < 1.5 ‰$ ; Liu et al. (2021); Schmittner et al. (2013)).

#### 4.4 Evolution of pH, Total alkalinity, $\Sigma\text{CO}_2$ , silicates

During the ongoing eruption (May 2019), exceptional pH anomalies in water column up to -0.6 pH unit were measured both at the volcano summit and at the northern flank, for seawater samples taken below 2500 m (Figure 6; Table 3). Only one comparable anomaly was detected again, in July 2019 above the recent western lava flow, and was located between 3150 m deep and the seafloor (~ 3200 m). The strong pH anomalies observed during the eruption, are associated with a net increase in  $\Sigma\text{CO}_2$ ,  $A_T$  and  $\text{SiO}_2$ , compare to background levels and to the other studied casts. Maximum  $\Sigma\text{CO}_2$  of 2489  $\mu\text{mol/L}$  has been observed at 2640 m deep, above the volcano summit in May 2019. Similar anomalies up to 2434  $\mu\text{mol/L}$  were also observed during the eruption, above the northern flank but at deeper depths (~ 3160 m). This last anomaly level was found again in October 2020, at the same depth, above the active northwest lava flow. The strongest alkalinity addition happens during the eruption at the volcano summit, with concentrations up to 2700  $\mu\text{mol/L}$ , associate to a strong silicate addition, up to 20  $\mu\text{mol/L}$ .

In May 2019, while the strong anomalies are located below 2000 m depth, the entire water column seems to be impacted by the eruption with pH,  $\Sigma\text{CO}_2$  and  $A_T$  levels outside the background envelope. July 2019 and October 2020 values, except for the few anomalies mentioned above, show moderate anomalies localized below 2000 m, with an acidification that does not exceed 0.3 pH unit, and  $\Sigma\text{CO}_2$ ,  $A_T$  and  $\Delta\text{SiO}_2$  up to 2370  $\mu\text{mol/L}$ , 2490  $\mu\text{mol/L}$  and 14  $\mu\text{mol/L}$ , respectively. Overall, anomaly levels were stronger in May 2019 than July 2019, which were themselves stronger than October 2020 levels.

#### 4.5 Evolution of TDFe and TDMn

Whatever the sampling date or location, depth profiles of TDMn and TDFe (Figure 7.A and B) show a similar trend with elevated concentrations below 2000 m deep compared to the local background, and with a strong enrichment near the seafloor (i.e. within the last 100 meters). The upper part of the water column presents low TDMn and TDFe concentrations (TDMn < 10 nmol/L ; TDFe < 200 nmol/L), close to background level. Depth profiles of TDMn and TDFe concentrations are indeed well correlated to those of  $^3\text{He}_{\text{xs}}$  and  $\text{CH}_4$  (see supplementary material \_ Figure 04). Maximum TDMn and TDFe concentrations at the seafloor were of 560 nmol/L and 10575 nmol/L, respectively, found during the May 2019 eruption, above the northern flank of the edifice (at 3100 m deep). Shallower in the water column (i.e., between 2000 m and 3100 m), maximum TDMn and TDFe concentrations above lava flows were up to 160 nmol/L and 2380 nmol/L, respectively. Concentration levels decrease from hydrocasts taken in May 2019 to those taken in October 2020. Nonetheless, maximum TDMn and TDFe concentrations measured during the last cruise were still out of the background envelope with respective values up to 80 nmol/L and 880 nmol/L at 3000 m deep, and up to 120 nmol/L and 1880 nmol/L close to the seafloor (3260 m).

The significant correlation between iron and manganese concentrations allows to define a range of TDFe/TDMn ratios between ~11 and ~27 (Figure 7.C<sub>1</sub> and C<sub>2</sub>). Elevated ratios were measured at deep water layers, close to the seafloor and near the surface of the volcano walls. The maximum TDFe/TDMn ratio of ~27 was found above the northern flank in May 2019 at depths between 3025 and 3110 m (MAY01-HY03), and was measured again in July 2019 at the same location for equivalent depths (cast MAY04-HY04). Within the layer from 2600 m to 2900 m deep, lower values of ~22 are measured in May 2019 and ~20 in July 2019. Molar ratios from ~27 to ~20 were respectively measured from right above the volcano summit (at

~2720 m) to shallower depths (~ 2590 m) during the May 2019 eruption (cast MAY01-HY02). This ratio also decreases with decreasing sampling depth, with values from ~15 to ~11 for depths between 2500~2400 m. Intermediate ratios between ~14 and ~18 were found above the recent western lava flow in July 2019 (MAY04-HY07, MAY04-HY09) and the very recent northwest lava flow in October 2020 (MAY15-HY06). Although samples for the later hydrocast spread along a ratio of ~16, depletions in TDFe are observed giving a ratio of ~11 at 2894 and 3002 m. Samples above the active northwest lava flow (cast MAY15-HY08) also exhibit a ratio of ~11, with the deepest sample (3260 m) that highlight a different pattern with a ratio of ~16.

## 5 DISCUSSION

### 5.1 Rapid shift in magmatic fluid contribution

Fluid emissions at the seafloor are a source of helium to the water column, being either primordial ( $^3\text{He}$ ) or radiogenic ( $^4\text{He}$ ). Mantle and crustal contributions of these fluids are defined by the corrected isotopic helium ratio relative to the atmospheric ratio ( $R_c/R_a$ ). Mantle MORB-like fluids are usually described by  $R_c = 8.0 \pm 1.5 R_a$  and  $^4\text{He}/\text{Ne} = 1000$  (Sano and Fischer, 2015), while fluids originating from the crust present  $R_c$  values of  $0.02 R_a$  and  $^4\text{He}/\text{Ne}$  values of 1000 (Wang et al., 2020). Air saturated seawater (ASW) is defined by  $R_c = 1 R_a$  and  $^4\text{He}/\text{Ne} = 0.226$  (Hilton, 1996; Weiss, 1971). Therefore, a corrected ratio ( $R_c/R_a$ ) close to 8 in seawater would imply that He source is dominated by a mantle-derived contribution with negligible assimilation of crust-derived materials which may occur during magma aging and/or interactions with  $^4\text{He}$ -rich crustal rock, also referred as country rock (Hilton et al., 1993).

During the main eruptive event in May 2019, the magmatic contribution to the water column remains unknown as no helium isotope measurement were made at this time. However, a recent geochemical study of volcanic rocks from the volcano shows no evidence for crustal material assimilation, which could be explained by a direct and fast ascent of magma from the deep reservoir to the surface (Berthod et al., 2021). We however observe a change in magmatic fluid contribution (Figure 8) between seawater samples taken above the recent western lava flow in July 2019 (casts MAY04-HY04 and MAY04-HY07) and those taken above the northwest active and very recent lava flow from October 2020 (casts MAY15-HY06 and MAY15-HY08). Extrapolating  $R_c$  values in our samples using the linear regressions in Figure 8.A, down to a null  $Ne/He$  ratio, we approximate  $R_{c,fluid}$  values. Such extrapolated  $R_{c,fluid}$  values of 6.46 Ra in July 2019 suggest a higher crustal (i.e. radiogenic) contribution compared to October 2020 (extrapolated  $R_{c,fluid} = 8.52$  Ra). Evidence for significant crustal material assimilation in the magmatic source in July 2019 is supported by petrogeochemical studies that have also shown a more crustal signature in those lavas. Authors explain this signature by the sampling of an evolved magma batch (i.e. that has assimilated crustal material during its aging), located on the magma path, during the magma ascent from the main reservoir to the seafloor (Berthod et al., 2021). In October 2020, the return to less radiogenic (more primordial) helium signatures might be linked either to (i) a new magma path with direct ascent from the main reservoir to the seafloor, as seen in May 2019, or (ii) the passage of the magma through the same conduit as in July 2019 but with the secondary magma reservoir empty or newly recharged, and therefore no crustal assimilation (Berthod et al., 2022).

The measured helium water column composition yield the same range of  $R_c/R_a$  as Mayotte gaseous emissions in Petite-Terre ( $R_c/R_a = 6.4-7.5$ ; (Liuzzo et al., 2021)) and Indian Ridge hydrothermal fluids ( $R_c/R_a = 7.8-8.0$ ; (Gamo et al., 2001; Kawagucci et al., 2008)).

Assuming that dissolved gas sources from the volcano exhibit a mantle MORB-like signature of  $R_c = 8.0 \pm 1.5 R_a$  (Sano and Fischer, 2013), we estimate from the isotopic helium ratios that the level of crustal contamination could be between 20~35 % in July 2019 (Figure 8). However, this interpretation does not take into account the possible influence of the La Réunion hotspot where magma sources present  $R_c/R_a$  with a range from 12 to 14.5 (Bouidoire et al., 2020; Marty et al., 1993). At this stage, as it was suggested by the recent studies (Famin et al., 2020; Lemoine et al., 2020; Michon, 2016; Tzevahirtzian et al., 2021), we hypothesize that there is no influence of this hotspot on Mayotte submarine eruption.

## **5.2 Origin of contrasted behavior of gases**

Using seafloor observations (SCAMPI pictures, Table 1) and turbidity signals (Figure 2), we interpret the geochemical anomalies in the water column according to two parameters: the freshness of lava, i.e., indicating the timing between lava flow emplacement and water column sampling; and the potential seawater-rock-lava interaction and their associated fluid emissions.

### **5.2.1 Ongoing eruption and active lava flow**

#### **5.2.1.1 Elevated $H_2$ levels**

Exceptionally high  $H_2$  concentrations were measured during the eruption (inside the acoustic plume, in May 2019) and above active lava flow (in October 2020), up to 5993 nmol/L and 648 nmol/L respectively.

Hydrogen is usually described as an immediate tracer of the eruptive activity and provides strong evidence for on-going or very recent reactions between seawater or magmatic water and molten or extremely hot rocks (Baker et al., 2011; Baumberger et al., 2020; Baumberger et al., 2014; Resing et al., 2011). Indeed, in marine environments,  $H_2$  is produced from

various sources, involving abiotic and biotic processes (Wang et al., 2023; Worman et al., 2020). In volcanic environments, with large magma inputs such as fast-spreading mid-ocean ridges or intraplate or hotspot volcanoes, hydrogen may originate from magmatic degassing as a result of magma crystallization, through the oxidation of ferrous iron contained within the magma by reduction of dissolved water (Hekinian et al., 1973; Klein et al., 2020; Symonds et al., 1994).  $H_2$  may also be produced through the interaction between molten lava and seawater (Sansone and Resing, 1995), and more generally through the reduction of water during the oxidation of Fe(II)-bearing rocks (Truche et al., 2020). Indeed, some of the  $H_2$  we observe might come from high temperature basalt alteration. During the high-temperature ( $\sim 350$  to  $400$  °C) alteration of oceanic crust by seawater, the majority of ferrous silicates alter to ferrous iron minerals (e.g., chlorite, amphibole), however, a small number, alter to ferric-bearing minerals and produce  $H_2$ . Other major sources of hydrogen in the ocean include the radiolysis of water due to radioactive decay of U, Th and K; crustal weathering or reaction of water with surface radicals during fracturing of silicate-bearing rocks (Klein et al. 202, Wang et al, 2023), all occurring in very distinct geological settings than ours. Decomposition of organic matter in sediment-hosted systems has also been reported, but is very unlikely as sediment both in the lagoon and offshore Mayotte are mainly carbonateous with very low organic carbon contents (Dullo et al., 1998; Zinke et al., 2003b).

Production of hydrogen through serpentinization of ultramafic materials (i.e. hydration reactions of olivine and pyroxene, mostly) is very common in submarine settings. This mechanism is generally considered to be the main  $H_2$  production route during hydrothermal circulation at slow and ultra-slow spreading ridges (e.g. Charlou et al. (2010)). The geological context here is of course very distinct and we did not find evidence, neither from dredge operations nor from direct seafloor observations, that would support exhumation of ultramafic materials. Although we cannot exclude a mechanism in which seawater is interacting at



greater depth with ultramafic rocks, it should be noted that H<sub>2</sub> generation through serpentinization likely requires a mature hydrothermal system, which seems to be in contradiction with the young age (< 1 years) and the transient nature of the H<sub>2</sub> anomalies observed in the water column.

We therefore propose that H<sub>2</sub> is produced both from magmatic degassing and from water reduction by iron-bearing compounds in the extruding high temperature lava during its interaction with seawater, following the reaction (Baker et al., 2011; Perfit et al., 2003; Worman et al., 2020):  $2(\text{FeO})_{\text{magma}} + (\text{H}_2\text{O})_{\text{seawater}} \rightarrow (\text{Fe}_2\text{O}_3)_{\text{rock}} + \text{H}_2$ . Following its production, H<sub>2</sub> is likely to be consumed by oxidation through abiotic reactions or microbial processes, usually within the timespan of a few hours to a few days (McLaughlin-West et al., 1999; Worman et al., 2020).

Clague et al. (2009) documented submarine eruptions throughout the Pacific Ocean at depths from 1400 to 3800 m, and reported that an almost unfailing characteristic of submarine eruptions is the production of glassy pyroclastic fragments that are remnants of bubbles of magmatic gas. Also, Baker et al. (2011) showed that the production of pyroclastic fragments promotes extensive lava-seawater interaction during the eruption. At Mayotte submarine volcano, very fresh basaltic pillow lavas were dredged on the northeastern flank of the edifice and contain significant amounts of vesicle-trapped volatiles (Berthod et al., 2021; Feuillet et al., 2021). Such vesicular and gas-rich rocks, referred as 'popping rocks', may therefore provide larger effective surface area for seawater-lava interactions.

Additionally to the gas-rich characteristic of the rocks, the extremely high concentrations of H<sub>2</sub> probably testify for the explosive character of the Mayotte submarine eruption, as previously proposed by Baumberger et al. (2014) during the West Mata eruption and by Baumberger et al. (2020) during the Puipui eruption. Submarine eruptions may generate

massive megaplumes, of several kilometers height, as a the result of extremely high rates of energy discharge, including massive heat and magmatic and/or crustal fluids transfer (Baker et al., 2012; Pegler and Ferguson, 2021). Large fluxes of H<sub>2</sub> may have therefore been discharged into the water column as a result of a gas jet formation.

### 5.2.1.2 Elevated CO<sub>2</sub> and CH<sub>4</sub> levels

During the eruption, elevated concentrations of CO<sub>2</sub> and CH<sub>4</sub> were released, up to 265 µmol/L and 821 nmol/L, respectively. This positive correlation between CO<sub>2</sub> and CH<sub>4</sub> values might suggest a magmatic origin for both these gases. Carbon dioxide is most likely sourced from lava outgassing (Craig and Lupton, 1981), while methane may be present as a magma volatile or could reflect a production through Fischer-Tropsch-type reactions ( $\text{CO}_2 + 4\text{H}_2 \rightleftharpoons \text{CH}_4 + 2\text{H}_2\text{O}$ ) associated with water-rock interactions (Craig, 1953; McCollom, 2013; Zolotov and Shock, 2000).

The carbon dioxide is one of the main volatiles dissolved in magma along with H<sub>2</sub>O and SO<sub>2</sub>. During the magma ascent, gas bubbles can segregate from the melt at different depths, so the volatile components fractionate according to their solubilities. The composition of the exsolved fluids will thus change as a function of the pressure-related solubility of each volatile species. Being the CO<sub>2</sub> less soluble in the melt than water, it will be exsolved at deeper levels (Métrich and Wallace, 2008). Because the exsolved fluids are less dense than the melt they ascent faster to the surface, leading to fluid emissions with a very high concentration in a specific volatile, that may be varying in time and space. Thus, CO<sub>2</sub> may be generated through a separate CO<sub>2</sub>-rich gas phase directly degassing from the magma chamber, as it was observed at NW Rota-1, where CO<sub>2</sub>-rich gas bubbles exsolve from slowly erupting lava (Chadwick et al., 2008). When the CO<sub>2</sub>-rich gas phase encounters circulating seawater during its ascent through the volcano edifice, a two-phase mixture of CO<sub>2</sub>-rich gas and an

aqueous phase undersaturated with  $\text{CO}_2$  can coexist as buoyant gas bubbles ascend through and exchange with the aqueous phase (Lupton et al., 2008). The behavior of  $\text{CO}_2$  released into seawater will be governed primarily by the pressure (i.e., depth) and temperature of the water entity into which it is released, and to a lesser extent its salinity. Taking into account the salinity and temperature profiles of seawater obtained in the area with our CTD casts,  $\text{CO}_2$  will become liquid at pressures of 45–50 bar, corresponding to water depths of ~450–500 m (Figure 9). Above ~2700 m depth, density of liquid  $\text{CO}_2$  is lower than the seawater density. When released into the water column at this depth or shallower,  $\text{CO}_2$  will hence rise towards the surface. On the contrary, the  $\text{CO}_2$  emitted below ~2700 m depth will likely sink to the ocean floor. This threshold of 2700m corresponding to the summit depth of the Fani Maore volcano, we suggest that a significant amount of  $\text{CO}_2$  emitted during the eruption sank and generated the high concentrations we observe at the bottom and the flanks of the volcano (Figure 9).

Eruptive megaplumes may involve the rapid evacuation of existing intracrustal fluid reservoirs (Baker et al., 2012; Lupton et al., 1999; Pegler and Ferguson, 2021). Such syn-eruptive release of mature hydrothermal fluids enriched in methane are usually observed in extensional tectonic settings, which promotes seafloor hydrothermal circulation and may be significantly enhanced by dyke intrusions (Curewitz and Karson, 1998; Delaney et al., 1998; Pegler and Ferguson, 2021). However, we did not find any signs of pre-eruptive hydrothermal active venting on the seafloor images we collected (no vent fauna, no sulfide deposits, no smokers, only surficial oxy-hydroxydes iron deposits on some of the freshly extruded lava flows). Although we cannot rule it out, it seems therefore unlikely that the concurrent release of significant crustal fluids as the generation process for methane was solely responsible for the elevated anomalies we observed during the eruption. Given the low organic matter content

of the sediments in the area (Manoux et al., 2023), thermogenic cracking of organic matter during the magma ascent might not act as a significant source of methane released during the eruption.

Journal Pre-proof

**5.2.1.3 A common pathway invoked for the formation of hydrocarbons and other organic compounds in geologic environments is the Fischer-Tropsch synthesis (McCollom, 2013). As originally described, Fischer-Tropsch type chemical reactions refer to the surface-catalyzed reduction of CO by H<sub>2</sub> in gas mixtures. In geological systems, dissolved CO<sub>2</sub> may be considered the primary carbon source for such abiotic organic synthesis (McCollom, 2013; Zolotov and Shock, 2000). Yet, despite a thermodynamic thrive for CO<sub>2</sub> reduction into CH<sub>4</sub> in conditions of hydrothermal circulation, it is now recognized that the process is likely slow and inhibited by strong kinetic barriers. For the process to overpass these kinetic barriers and produce significant amount of reduced carbon compounds such as methane (McCollom, 2016; McDermott et al., 2015), it may requires the presence of metal catalysts or of a co-existing H<sub>2</sub> rich gas phase (McCollom, 2016). Although speculative at this stage, we note that one or both of these conditions could be met in the case of the Fani Maoré eruption. First, the presence of large TDFe anomalies in the water-column supports sustained interactions of seawater with Fe-bearing phases that could act as catalyst for a Fischer-Tropsch type reaction. On the other hand, given the depth of Fani Maoré eruption, liquid and gaseous phases probably coexisted. Taken together, we thus suggest that Fischer-Tropsch type reaction is a potential mechanism for the formation of methane observed in the water column. Why such a dichotomy between H<sub>2</sub> versus CO<sub>2</sub>, CH<sub>4</sub> profiles at the edifice?**

During the eruption, concentration profiles of CH<sub>4</sub>, CO<sub>2</sub> and H<sub>2</sub> were studied at two locations in the vicinity of the volcano: at the summit and above the northern flank (Figure 4). From the water surface down to 2500 m depth, CH<sub>4</sub> and CO<sub>2</sub> concentrations are similar to those found in the local background. Below 2500 m, concentrations of both CH<sub>4</sub> and CO<sub>2</sub> increase, with maximum values at the seafloor. However, H<sub>2</sub> displays the opposite trend; very

high anomalies (up to 6  $\mu\text{mol/L}$ ) are seen at depths above 2500 m while  $\text{H}_2$  concentrations oscillate between 11 and 56  $\text{nmol/L}$  below 2500 m. To our knowledge, such dichotomy in gas behavior between  $\text{H}_2$  on one hand and  $\text{CO}_2$  and  $\text{CH}_4$  on the other hand, has never been reported before in a context of deep submarine eruption. A plausible explanation is related both to different processes of gas generation and to the change in density equilibrium between liquid  $\text{CO}_2$  and seawater around 2700 m depth (Figure 9):

- On one hand,  $\text{H}_2$  is generated as a free gas during lava quenching, i.e. at the exit point of the magma at the summit (2600~2700 m).  $\text{H}_2$  dissolves in seawater and rises the water column, probably encouraged by the formation of a gas jet (Cahalan and Dufek, 2021). We observe no anomalies in potential temperature, potential densities (Supplementary Figure 2) nor turbidity anomalies (Figure 2) between 2500 and 1300m although we do see some high dissolved  $\text{H}_2$  concentrations randomly dispersed. Such features suggest that we did not capture the full tridimensional structure of the eruptive plume at these depths on this one cast (Pegler and Ferguson, 2021). The lower  $\text{H}_2$  concentrations measured between 2500-1300 m compared to the very elevated one at 1000m may therefore simply result from the CTD-rosette emplacement outside the plume due to local currents and the turbulent 3D plume behavior.
- On the other hand,  $\text{CO}_2$  is discharged through magma degassing, either from the exit point at the summit, from lavas flowing down the volcano flanks, or from fractures on the volcano flanks. Since the seafloor around the Fani Maoré new volcanic edifice is around 3400-3600 m depth and the top of the volcano is around 2600-2700 m,  $\text{CO}_2$  emitted will likely sink to the ocean floor instead of rising up to the surface. At the same time, we expect that  $\text{H}_2$  is generated by lava-seawater interactions from the lavas flowing down the volcano flanks. As its concentration does not exceed 56  $\text{nmol/L}$  below 2500 m, we suggest that  $\text{H}_2$  is consumed by the Fischer-Tropsch-type chemical

reaction to generate  $\text{CH}_4$  through the reduction of  $\text{CO}_2$  (1 moles of dissolved  $\text{CO}_2$  react with 4 moles of  $\text{H}_2$ ). This reaction seems the most appropriate to explain why  $\text{H}_2$  is lower at the bottom of the water column than at shallower depths. However, in this study, we are not able to estimate the amount of methane generated through this reaction. We discard microbial consumption of hydrogen as a significant process as the rates at stake and their distribution in seawater cannot explain the discrepancy of hydrogen concentration over depth (Lappan et al., 2023).

Therefore, we suggest that the dichotomy in the generation processes of the various gases and the very specific settings of the Fani Maore volcano create a unique environment. At this stage of the eruption, past the initial eruptive outburst, lava are being emitted effusively from the summit down to the flanks (no explosive activity registered as turbidity anomalies are limited to 2500m ; Figure 2) :  $\text{CH}_4$  will likely be associated with the liquid  $\text{CO}_2$  released by the volcano whereas  $\text{H}_2$  will be released as a free gas in the water column. This would explain the high concentrations in methane found below 2500 m, while  $\text{H}_2$  tends to stay in the gas phase and rises to the surface giving place to the  $\text{H}_2$  anomalies aforementioned.

### 5.2.2 Continued lava flow

Above the northern flank, two months after the eruption,  $\text{CO}_2$  and  $\text{H}_2$  concentrations are back to background levels while  $\text{CH}_4$  concentrations remains elevated (100-200 nmol/L, Figure 5). Water column above the recent western lava flow (MAY04-HY07, MAY04-HY09) exhibit  $\text{CH}_4$  anomalies up to 777 nmol/L (Figure 5), which is more than twice the concentrations found above the very recent and active northwest lava flow for which maximum concentration was 284 nmol/L (Table 1).

In submarine volcanic systems, CH<sub>4</sub> is generally produced through hydrothermal circulation that is initiated after an eruptive event. Buck et al. (2018) have compiled maximum CH<sub>4</sub> concentrations measured in hydrothermal plumes found above Ahyi, NW Rota, West Mata, Nikko, Daikoku and Kasuga-2 and concentrations do not exceed 22 nmol/L (Baumberger et al., 2014; Buck et al., 2018; Resing et al., 2009; Resing et al., 2011). The low H<sub>2</sub> levels (i.e. only up to 40 nmol/L) measured above the lava flows compared to those measured right during the ongoing eruption may be due to the weakening of the lava-seawater interaction processes and to the rapid oxidation and consumption of H<sub>2</sub> produced through these processes (McLaughlin-West et al., 1999; Worman et al., 2020). Moreover, the elevated concentrations of CH<sub>4</sub> coupled with low concentrations of H<sub>2</sub> are consistent with a sudden release of subsurface fluids in which microbial processes could account for elevated CH<sub>4</sub> and low H<sub>2</sub>. An alternative source for CH<sub>4</sub> is thermogenic decomposition of buried organic matter following the eruption and/or subsurface methanogenesis (McLaughlin-West et al., 1999).

CO<sub>2</sub> was the dominant dissolved gas measured above the western recent lava flow (MAY04-HY07 and MAY04-HY09, July 2019), and the northwest very recent (MAY15-HY06, October 2020) and active (MAY15-HY08, October 2020) lava flows (Figure 5). Such emissions of CO<sub>2</sub> may originate from different sources such as mantle, oceanic crust, sedimentary carbonates and organic matter (de Hoog et al., 2001; Marty et al., 1989; Resing et al., 2007). The mean molar ratio of CO<sub>2</sub> to <sup>3</sup>He measured at the vicinity above recent (MAY04-HY07), very recent (MAY15-HY06) and active (MAY15-HY08) lava flows is at  $6.82 \pm 2.32 \times 10^9$ , which is elevated compared to the ratio found at the NW Rota-1 submarine volcano ( $3.25 \pm 0.07 \times 10^9$ , Resing et al. (2007)) or more generally at global magma outgassing at mid-ocean ridges ( $2 \times 10^9$ , Marty and Jambon (1987)). As it is also outside the range of mid-ocean ridge hydrothermal fluids ( $0.7$  to  $4.6 \times 10^9$ , Resing et al. (2004)), we argue that a hydrothermal fluid circulation is unlikely, or hasn't been emplaced yet, consistently



with the very young age of the volcano. Our value is however within the range of submarine arc volcanoes ( $12 \times 10^9$  at Suiyo seamount, Tsunogai et al. (1994) ;  $10 \times 10^9$  at NW Eifuku seamount, Lupton et al. (2006)) and subaerial arc volcanoes (about 6 to  $34 \times 10^9$ , Sano and Marty (1995)). Our value is also very similar to vent fluid value at Loihi seamount, where  $\text{CO}_2/{}^3\text{He}$  ratio changed rapidly (i.e. increased) following a seismic crisis (Hilton et al., 1998). As it was demonstrated by Marty et al. (1989) the apparent excess of  $\text{CO}_2$  relative to  ${}^3\text{He}$  cannot be entirely due to the physical or chemical fractionation occurring during the transfer of gases from the magmatic source to the surface. Hilton et al. (1998) have shown that the degassing of an alkalic magma may explain  $\text{CO}_2/{}^3\text{He}$  ratios (measured in fluids) higher than the initial magma ratio due to the solubility behavior of  $\text{CO}_2$  and He in magmas of different chemistry. In low- $\text{SiO}_2$  alkali basalts, the solubility of  $\text{CO}_2$  is significantly higher than in tholeiites, while helium solubility decreases with decreasing  $\text{SiO}_2$ . Thus, volatiles residual after a degassing event will have higher  $\text{CO}_2/{}^3\text{He}$ . A possible origin for excess carbon is the contribution (i.e. contamination) of carbonaceous sediments being a prominent source of  $\text{CO}_2$  under the appropriate T-P- $f_{\text{O}_2}$  conditions (Marty et al., 1989). However, even if the contribution of crustal gases was more elevated for July 2019 samples than for the October 2020 samples, we do not observe a significant change in  $\text{CO}_2/{}^3\text{He}$  values between those both periods. Therefore we attribute the excess in  $\text{CO}_2$  relative to  ${}^3\text{He}$  to an enrichment of  $\text{CO}_2$  originating likely from carbonates and organic matter of the thick sediment cover between the main volcanic layer, below the new volcano, and the top of the crust (2.2-2.5km, Masquelet et al. (2022a))

The  $\delta^{13}\text{C}\text{-CH}_4$  signatures of  $-34 \text{‰}$  in the water column are rather ambiguous and can point to both abiotic or thermogenic signature of methane (Etiope and Sherwood Lollar, 2013). Indeed, methane isotope signature observed in hydrothermal fluids from mid-ocean ridge regions, like the East Pacific Rise or Mid-Atlantic Ridge, generally display  $\delta^{13}\text{C}\text{-CH}_4$  values

between  $-8.6$  to  $-23$  ‰ and (Kawagucci et al., 2008; Sano and Fischer, 2013; Wen et al., 2016), and references therein). Our values are however more similar to warm vents and gas bubbles from back arc submarine volcano where  $\delta^{13}\text{C-CH}_4$  ranging from  $-24.8$ ‰ to  $-41.4$ ‰ have been reported and suggest a primarily thermogenic origin for  $\text{CH}_4$  (Michel et al., 2018).

With values of  $\delta^{13}\text{C-CH}_4 = -34.8$  ‰ and  $-34.0$  ‰ measured in July 2019, and October 2020 respectively, the stable carbon isotopic composition of methane measured in the water column above the Fani Maoré volcano falls in the range of  $-75$ ‰ to  $-15$ ‰ corresponding to early mature and very late mature thermogenic gases, but also within the  $-50$ ‰ to  $+10$ ‰ abiotic generation range (Milesi et al., 2020; Milkov and Etiope, 2018). Milkov and Etiope (2018) demonstrated that thermogenic gases are often mixed with microbial gases (in sediments at diagenetic to early catagenetic stages) and abiotic gases (e.g., in geothermal volcanic plumbing systems involving organic-rich rocks). The low organic carbon content of the sediment does not support extensive thermogenic generation of methane through magma/sediment interaction during the ascent. However, the volcano does lie above  $\sim 2.2$ - $2.5$  km thick sediment cover (Masquélet et al., 2022b), which depending on the magma ascent rate and conditions, may release enriched methane mature fluids of thermogenic signatures (Etiope and Sherwood Lollar, 2013; Pegler and Ferguson, 2021). With the current dataset, it is not possible to favor an abiotic over a thermogenic origin of  $\text{CH}_4$ .

### 5.3 Carbonate system response to high $\text{CO}_2$ discharges

Submarine volcanoes discharge acid-rich fluids (e.g. sulfuric acid originating from  $\text{SO}_2$  disproportionation),  $\text{CO}_2$  rich-fluids (e.g. magma  $\text{CO}_2$  volatile), and fluids rich in  $\text{CO}_2$  and alkalinity (e.g. mixture of magmatic volatiles and products of water/rock interactions). The addition of  $\text{CO}_2$  within the water column results in acidification of the seawater, whereas the addition of alkalinity increase the pH. When both  $\text{CO}_2$  and carbonate alkalinity are added, pH

decrease but less than when only CO<sub>2</sub> is added (Resing et al., 2009). Representation of the pH-CO<sub>2</sub> relationship as  $\Delta\Sigma\text{CO}_2$  against  $\Delta\text{pH}$  (delta values being the difference from the regional background) (Figure 10) displays the three trends that might explain the significant water column acidification (Figure 6): (1) CO<sub>2</sub> addition, (2) CO<sub>2</sub> and carbonate alkalinity addition, (3) mineral acid addition.

Samples taken above the northern flank during the eruption, between 2250 m and 2750 m depth (cast MAY01-HY03), exhibit a strong decrease in pH (-0.6 pH unit) that seems to be explained by an addition of CO<sub>2</sub> (showed by the red line in Figure 10). According to the gas behavior study, at these pressure and temperature conditions (5.2.1.), we suppose that the CO<sub>2</sub> was mainly in the form of liquid CO<sub>2</sub> rising up through the water column. The absence of carbonate alkalinity addition suggests a limited fluid-rock interaction. Indeed,  $\Sigma\text{CO}_2$  and  $A_T$  anomalies are just above the background level and the TDFe/TDMn ratio is about 2. Rather than originating from fluid-rock interaction, the significant anomalies in silicates we observe at the volcano northern flank ( $\Delta\text{SiO}_2$  up to 15  $\mu\text{mol/L}$ ) are likely due to basalt alteration at elevated temperature conditions. Indeed, as demonstrated by Resing et al. (2009), the presence of CO<sub>2</sub> without alkalinity suggests that the CO<sub>2</sub> does not react extensively with the host volcanic rocks to form alkalinity. Limited fluid-rock interaction is also consistent with the presence of pure CO<sub>2</sub> in liquid and clathrate forms that will limit CO<sub>2</sub> dissolution in seawater and facilitate CO<sub>2</sub> ascend in the water column due to density differences above 2700m (Figure 9), thus preventing extensive surface reaction with the volcanic rocks.

Deeper than 2750 m above the northern flank, for the same cast (MAY01-HY03), pH is mainly controlled by CO<sub>2</sub> addition but shows a potential carbonate alkalinity addition that suggests rock weathering processes. This hypothesis is supported by the observation of moderate  $\Sigma\text{CO}_2$  and  $A_T$  anomalies, the high TDFe/TDMn ratio of 27, and the significant

correlation between  $\Sigma\text{CO}_2$  and TDMn for this cast ( $r^2=0.82$ ,  $p<0.0001$ ). This fluid-rock interaction might be explained by the liquid  $\text{CO}_2$  that flows down the volcano flanks at these depths. Here, silicate anomalies are however lower, and can be explained by a lower temperature anomaly that does not enhance silicate alteration. The TDFe/TDMn ratio is similar to the one found at Ruby submarine volcano, at the Mariana arc (Fe/Mn = 26, Resing et al. (2009)), for which authors have attributed the elevated Fe levels to the carbonic acid dissolution of the host rocks as Ruby volcano shows evidence of being high alkalinity/high  $\text{CO}_2$  systems. This ratio is also consistent with the one of ~30 found in hydrothermal fluid from Pele's Vent (Loihi Seamount) where fluids were enriched in total dissolvable  $\text{CO}_2$  and was attributed to chemical weathering of wall rock by magmatic volatiles entrained in the circulating hydrothermal fluids (Glazer and Rouxel, 2009).

At the volcano summit, between 2250 and 2750 m deep, the ongoing eruption led to a moderate acidification of about -0.3 pH unit. This pH anomaly is associated with a significant increase in  $\Sigma\text{CO}_2$  ( $\Sigma\text{CO}_2 = 2644.2 \mu\text{mol/L}$ ), which seems to have enhanced rocks weathering processes as indicated by a strong silicate anomaly ( $\Delta\text{SiO}_2 = 20 \mu\text{mol/L}$ ) and elevated alkalinity values ( $A_T = 2650.6 \mu\text{mol/L}$ ). These maximum values of  $\Sigma\text{CO}_2$ ,  $\Delta\text{SiO}_2$  and  $A_T$  are found at 2703 m, just above the summit and are associated with elevated TDFe/TDMn ratios of about 27, which is consistent with the hydrothermal fluid ratio value (i.e. ~30) from Pele's Vent (Loihi Seamount) where fluids were enriched in total dissolvable  $\text{CO}_2$ , as previously describe. At 2250 m, this ratio decreases down to 11, as well as  $\Sigma\text{CO}_2$ ,  $\Delta\text{SiO}_2$  and  $A_T$  anomalies that decrease toward the background level. These observations seems to highlight the presence of strong water-rock interactions close to the summit of the volcano, which may have been enhanced by high temperature conditions during the ongoing eruption.

Higher than 2250 m in the water column, at the summit and above the northern flank during the ongoing eruption, pH anomalies are lower with maximum values of -0.26 pH unit, and seems to result both from CO<sub>2</sub> addition and carbonate alkalinity addition (brown arrow in Figure 10). Actually, the majority of our samples (all cruises and casts) displays a pH that seems to be controlled by additions of both CO<sub>2</sub> and carbonate alkalinity. We suggest here, that acidification originates from the discharge through the water column of fluids rich in liquid CO<sub>2</sub> that slowly dissolves in seawater. This seawater, enriched in CO<sub>2</sub>, then reacts with volcanic rocks to generate carbonate alkalinity and reach the carbonate equilibrium. This process might have occurred in contact with the seafloor, lava flows and volcano flanks, and got diluted when moving up into the water column. Such hypothesis is consistent with the low concentrations of TDFe and TDMn, and low anomalies of  $\Sigma\text{CO}_2$ ,  $\Delta\text{SiO}_2$  and  $A_T$  observed above 2250m above the volcano.

Samples taken above the western recent, and the northwest very recent and active lava flows display anomalies of pH,  $A_T$ , SiO<sub>2</sub> and  $\Sigma\text{CO}_2$  located below 2250 m deep that are moderate to low, and that even reach the background envelope (as the  $\Delta\text{SiO}_2$  value for the northwest very recent lava, cast MAY15-HY06). The TDFe/TDMn ratios range between 17 and 11, and are lower than during the eruption. This ratio value corresponds to the NW Rota-1 ratio of 17 from Resing et al. (2009), where high acidity of fluids venting from the volcano likely dissolved the host rock, producing fluids with elevated TDFe/TDMn. The depletion of TDFe from hydrocasts sampled above the recent lava flows compared to hydrocasts performed at the edifice during May 2019 eruption is either due to a decrease of the emitted TDFe or to the iron precipitation over time.

Some samples taken above the western recent (MAY04-HY09) and the northwest very recent (MAY15-HY06) lava flows align themselves along the blue arrow on Figure 10. In particular,

the sample taken at 3154 m above the western recent lava flow (MAY04-HY09) presents an acidification of -0.5 pH unit that is not linked with the total alkalinity and silicates. This behavior suggests that the acidification is controlled by the addition of mineral acid ( $H^+$ ) likely generated by the emission of sulfur dioxide ( $SO_2$ ) that produces sulfuric acid ( $H_2SO_4$ ). In previous studies on submarine volcanoes at Mariana arc, authors determine that the mineral acidity ( $H^+$ ) originates from the  $SO_2 + H_2O = HSO_3^- + H^+$  reaction, when magmatic gases rich in  $SO_2$  come in contact with water (Butterfield et al., 2011; Resing et al., 2009; Resing et al., 2007). In our study, we suggest that this reaction might have occurred right above the emitted lava flows, implying the presence of magmatic gas rich in  $SO_2$ .  $H_2S$  which is also likely to be emitted during magma degassing may also generate acidity during its oxidation in the water column (e.g. Cline and Richards (1969)).

The major part of the samples taken above the lava flows, display pH and total dissolved inorganic carbon anomalies resulting from  $CO_2$  and carbonate alkalinity addition. Even if effusive activity was detected at the northwest active lava flow (cast MAY15-HY08), acidification does not exceed -0.1 pH unit and the addition of  $CO_2$  is also weak ( $< 70 \mu\text{mol/L}$ ). Only one deeper sample (3259 m) appears to be strongly enriched in  $CO_2$  ( $\Sigma CO_2 = 274.2 \mu\text{mol/L}$ ) but displays a weak pH acidification (-0.08 pH unit). This is likely due to a possible rock weathering occurring during the contact between fluid and seafloor. This anomaly is coupled with a relatively high TDFe/TDMn ratio ( $\sim 16$ ) and a slight increase of  $\Delta SiO_2$  even if this value stays within the background envelope. In gas-rich hydrothermal systems,  $H^+$  reacts first with the host rock followed by a  $CO_2$ -weathering reaction that produces alkalinity as  $HCO_3^-$ . The presence of alkalinity in deep samples collected above lava flows is consistent with long reaction paths where  $H^+$  is completely consumed and  $CO_2$  reacts with the host rocks (Resing et al., 2009).

Looking at the entire data set, the decrease of the overall eruptive activity intensity offshore Mayotte is clear during the investigated period. Indeed, even if lava flows from October 2020 are very recent and active, anomalies of pH,  $A_T$ ,  $SiO_2$  and  $\Sigma CO_2$  are smaller than those measured in July 2019 above recent lava, which are themselves lower than those from May 2019. Concentrations of TDFe and TDMn are also decreasing over time. Therefore, after the eruption, the carbonate system seems to be back to steady-state highlighting either (i) that the initial eruptive impact has been exported/flushed away due to deep current, (ii) or that the impact has been indeed buffered within the seawater column environment. To answer this, models of the dissolution of  $CaCO_3$  using water column geochemistry and/or correlation with local sediments analyses could be made. Although discharges of  $CO_2$  at the deep Fani Maoré submarine volcano have generated a locally confined ocean acidification (< 27000 km<sup>2</sup>) that decrease over time (i.e. returning to a steady-state) over a few months, biological impacts on organisms incorporating calcium carbonate into their structures cannot be excluded.

## 6 CONCLUSION

The compilation of geochemical data from Fani Maoré submarine volcano has provided valuable information about the setup of a volcanic edifice and the impact of an eruptive activity on the water column at a local scale. This study leads to the following conclusions:

- (1) The turbidity signals translate the decrease of the eruptive activity intensity from May 2018 to October 2020 (about 30 months), starting from a strong eruptive event at the volcano summit to continued lava flow emplacement.
- (2) A magma signature shift happens from crustal contamination to (pure) mantle signature between the western recent lava flow seen in July 2019, and the very recent and active northwest lava flow seen in October 2020. This highlights a

change to a direct magma ascent from the main reservoir to the seafloor, or a rapid recharge of the secondary magma reservoir.

- (3) The May 2019 eruption has generated, by seawater-lava interaction and probably encouraged by the formation of a gas jet, a strong H<sub>2</sub> discharge nearly 1000 m high within the water column above the volcano summit. Due to temperature and pressure conditions above the volcano flanks, CO<sub>2</sub> was emitted in liquid phase and sank for depths less than about 2680 m. A strong acidification of the water column was linked to the high discharge of inorganic carbon to the water column. Fluids, including liquid CO<sub>2</sub>, has interacted with the volcano walls producing high levels of metals, and elevated TDFe/TDMn ratios.
- (4) The lava flows around the volcano edifice has generated significant gas inputs near the seafloor. H<sub>2</sub> levels highlighted the recent eruptive activity, produced through lava quenching, and was then rapidly found at low levels due to oxidation and microbial consumption. CO<sub>2</sub> was released by magma outgassing through a longer time scale. Origin of methane released is more ambiguous. Indeed, although magma outgassing as a methane source is obvious in this context, release of a more mature crustal fluid, originating from the thermogenic cracking of sedimentary organic matter during the magma ascent may also occur given the thick sediment cover that the volcano penetrated. Fluids emissions to the water column have led to a moderate acidification of the seawater mainly resulting from the addition of dissolved inorganic carbon and the addition of carbonate alkalinity released by rock weathering processes. Significant acidification for a part of the deep-water samples above lava flows appears to be controlled by the addition of mineral acid (H<sup>+</sup>) from fluids rich in SO<sub>2</sub> and/or H<sub>2</sub>S.



- (5) About a year after the main eruptive event, with a decrease of the eruptive activity, the system appears to be approaching a steady-state where pH and total carbon values are heading towards the evaluated local background.
- (6) What is still unclear is whether this phenomenon is due to the decrease of the activity coupled with a renewing a water by the currents or to the buffering capacity and the resilience of the water column. To resolve this, future work could therefore focus on models of geochemical behavior of the water column under different scenarios and compare to sediment analyses or  $\text{CaCO}_3$  investigation.

Besides the geological context that obviously drives the type of volcanism and emissions of associated magmatic volatiles, our findings clearly highlights how environmental settings (e.g. depth, morphobathymetry) might shape the manifestations of submarine eruptions and its impact on the water column. In addition to play a significant part in the eruption mode (Cas and Simmons, 2018), the hydrostatic pressure clearly constrains the behavior of magmatic or eruption-driven volatiles such as  $\text{H}_2$ ,  $\text{CO}_2$  or  $\text{CH}_4$ , and, therefore, how they affect the adjacent marine pelagic and benthic ecosystems.

## 7 ACKNOWLEDGMENTS

We thank the crew members of the R/V Marion Dufresne (TAAF/IFREMER/LDA) and its Captain A. Eyssautier. We thank N. Feuillet, Y. Fouquet, E. Rinnert and I. Thinon the chief scientists of the MAYOBS01 cruise (May 2019, doi: 10.17600/18001217), the MAYOBS04 cruise (July 2019, doi: 10.17600/18001238), and the MAYOBS15 cruise (July 2019, doi: 10.17600/18001745). We also thank all the scientists involved. We thank Jürgen Sültenfuß from the Institute of Environmental Physics/Section of Oceanography at the University of

Bremen who performed all helium and neon isotopic analyses. We thank Bart van der Haven from Isolab b.v. who carried out the carbon isotope analyses.

## 8 FUNDING SOURCES

*MAYOBS1* campaign was funded by the CNRS-INSU TELLUS Mayotte program (SISMAYOTTE project). *MAYOBS4* and *MAYOBS15* campaigns were conducted by several French research institutions and laboratories (IPGP/CNRS/BRGM/IFREMER) and were funded by the Mayotte volcanological and seismological monitoring network (REVOSIMA, doi: 10.18715/MAYOTTE.REVOSIMA), a partnership between the Institut de Physique du Globe de Paris (IPGP), the Bureau de Recherches Géologiques et Minières (BRGM), the Observatoire Volcanologique du Piton de la Fournaise (OVVPF-IPGP), the Centre National de la Recherche Scientifique (CNRS), and the Institut Français de Recherche pour l'Exploitation de la Mer (IFREMER). This study was funded by the REVOSIMA, IFREMER and TotalEnergies as part of the MAYFIJUL PhD project (TOTAL ENERGIES FR000063751 // IFREMER 20/1001730).

## 9 APPENDIX A. SUPPLEMENTARY MATERIAL

Supplementary material presents vertical profiles of hydrographic parameters, and figure highlighting anomalies of potential temperature during the eruption and above the studied lava flows. Evaluation of background geochemistry is also presented through depth profiles. The relationship between TDMn, CO<sub>2</sub> and CH<sub>4</sub> with <sup>3</sup>He<sub>xs</sub> are provided in this file.

## 10 DATA AVAILABILITY

All data used in this study are presented in the tables, and/or will be deposited in SEANOE and SISMER online data repository.

## 11 REFERENCES

- Aminot, A., Kérouel, R., 2007. Dosage automatique des nutriments dans les eaux marines: méthodes en flux continu. Editions Quae.
- Archer, D.G., 1992. Thermodynamic Properties of the NaCl+H<sub>2</sub>O System. II. Thermodynamic Properties of NaCl(aq), NaCl·2H<sub>2</sub>O(cr), and Phase Equilibria. *Journal of Physical and Chemical Reference Data*, 21(4): 793-829.
- Assayag, N., Rivé, K., Ader, M., Jézéquel, D., Agrinier, P., 2006. Improved method for isotopic and quantitative analysis of dissolved inorganic carbon in natural water samples. *Rapid Communications in Mass Spectrometry*, 20(15): 2243-2251.
- Baker, E.T. et al., 2012. Hydrothermal Discharge During Submarine Eruptions The Importance of Detection, Response, and New Technology. *Oceanography*, 25(1): 128-141.
- Baker, E.T. et al., 2011. Unique event plumes from a 2008 eruption on the Northeast Lau Spreading Center. *Geochemistry, Geophysics, Geosystems*, 12(9).
- Barry, P.H. et al., 2020. Volatile sources, sinks and pathways: A helium-carbon isotope study of Baja California fluids and gases. *Chemical Geology*, 550: 119722.
- Baumberger, T. et al., 2020. Dissolved Gas and Metal Composition of Hydrothermal Plumes From a 2008 Submarine Eruption on the Northeast Lau Spreading Center. *Frontiers in Marine Science*, 7.
- Baumberger, T. et al., 2014. Understanding a submarine eruption through time series hydrothermal plume sampling of dissolved and particulate constituents: West Mata, 2008-2012. *Geochemistry, Geophysics, Geosystems*, 15(12): 4631-4650.
- Benson, B.B., Krause, D., 1980. Isotopic fractionation of helium during solution: A probe for the liquid state. *Journal of Solution Chemistry*, 9(12): 895-909.
- Berthod, C. et al., 2022. Temporal magmatic evolution of the Fani Maoré submarine eruption 50 km east of Mayotte revealed by in situ sampling and petrological monitoring. *Comptes Rendus Géoscience*, 354(S2): 195-223.
- Berthod, C. et al., 2021. The 2018-ongoing Mayotte submarine eruption: Magma migration imaged by petrological monitoring. *Earth and Planetary Science Letters*, 571: 117085.
- Boudoire, G., Rizzo, A.L., Arienzo, I., Di Muro, A., 2020. Paroxysmal eruptions tracked by variations of helium isotopes: inferences from Piton de la Fournaise (La Réunion island). *Scientific Reports*, 10(1).
- Buck, N.J., Resing, J.A., Baker, E.T., Lupton, J.E., 2018. Chemical Fluxes From a Recently Erupted Shallow Submarine Volcano on the Mariana Arc. *Geochemistry, Geophysics, Geosystems*, 19(5): 1660-1673.
- Butterfield, D.A. et al., 2011. High SO<sub>2</sub> flux, sulfur accumulation, and gas fractionation at an erupting submarine volcano. *Geology*, 39(9): 803-806.
- Cahalan, R.C., Dufek, J., 2021. Explosive Submarine Eruptions: The Role of Condensable Gas Jets in Underwater Eruptions. *Journal of Geophysical Research: Solid Earth*, 126(2).

- Cas, R.A.F., Simmons, J.M., 2018. Why Deep-Water Eruptions Are So Different From Subaerial Eruptions. *Frontiers in Earth Science*, 6.
- Cesca, S. et al., 2020. Drainage of a deep magma reservoir near Mayotte inferred from seismicity and deformation. *Nature Geoscience*, 13(1): 87-93.
- Chadwick, W.W. et al., 2008. Direct video and hydrophone observations of submarine explosive eruptions at NW Rota-1 volcano, Mariana arc. *Journal of Geophysical Research: Solid Earth*, 113(B8).
- Charlou, J.L. et al., 2010. High production and fluxes of H<sub>2</sub> and CH<sub>4</sub> and evidence of abiotic hydrocarbon synthesis by serpentinization in ultramafic-hosted hydrothermal systems on the Mid-Atlantic Ridge, Diversity Of Hydrothermal Systems On Slow Spreading Ocean Ridges, pp. 265-296.
- Charlou, J.L., Rona, P., Bougault, H., 1987. Methane anomalies over TAG hydrothermal field on Mid Atlantic Ridge. *Journal of Marine Research*, 45(2), 461-472.
- Clague, D.A., Paduan, J.B., Davis, A.S., 2009. Widespread Strombolian eruptions of mid-ocean ridge basalt. *Journal of Volcanology and Geothermal Research*, 180(2): 171-188.
- Clarke, W.B., Jenkins, W.J., Top, Z., 1976. Determination of tritium by mass spectrometric measurement of <sup>3</sup>He. *The International Journal of Applied Radiation and Isotopes*, 27(9): 515-522.
- Cline, J.D., Richards, F.A., 1969. Oxygenation of hydrogen sulfide in seawater at constant salinity, temperature and pH. *Environmental Science & Technology*, 3(9): 838-843.
- Craig, H., 1953. The geochemistry of the stable carbon isotopes. *Geochimica et Cosmochimica Acta*, 3(2): 51-92.
- Craig, H., Lupton, J.E., 1981. Helium-3 and mantle volatiles in the ocean and the oceanic crust. *The oceanic lithosphere*, 7: 391.
- Curewitz, D., Karson, J.A., 1998. Geological Consequences of Dike Intrusion at Mid-Ocean Ridge Spreading Centers, Faulting and Magmatism at Mid-Ocean Ridges, pp. 117-136.
- de Hoog, J.C.M., Taylor, B.E., van Bergen, M.J., 2001. Sulfur isotope systematics of basaltic lavas from Indonesia: implications for the sulfur cycle in subduction zones. *Earth and Planetary Science Letters*, 189(3): 237-252.
- Debeuf, D., 2004. Étude de l'évolution volcano-structurale et magmatique de Mayotte (archipel des Comores, océan Indien). Université de la Reunion, 277.
- Degens, E.T., Behrendt, M., Gotthardt, B., Reppmann, E., 1968. Metabolic fractionation of carbon isotopes in marine plankton—II. Data on samples collected off the coasts of Peru and Ecuador. *Deep Sea Research and Oceanographic Abstracts*, 15(1): 11-20.
- Delaney, J.R. et al., 1998. The Quantum Event of Oceanic Crustal Accretion: Impacts of Diking at Mid-Ocean Ridges. *Science*, 281(5374): 222-230.
- Dofal, A., Fontaine, F.R., Michon, L., Barruol, G., Tkalčić, H., 2021. Nature of the crust beneath the islands of the Mozambique Channel: Constraints from receiver functions. *Journal of African Earth Sciences*, 184: 104379.

- Donval, J.P., Guyader, V., 2017. Analysis of hydrogen and methane in seawater by "Headspace" method: Determination at trace level with an automatic headspace sampler. *Talanta*, 162: 408-414.
- Dullo, W.-C. et al., 1998. Morphology and Sediments of the Fore-Slopes of Mayotte, Comoro Islands: Direct Observations from a Submersible, Reefs and Carbonate Platforms in the Pacific and Indian Oceans, pp. 217-236.
- Embley, R.W. et al., 2014. Eruptive modes and hiatus of volcanism at West Mata seamount, NE Lau basin: 1996-2012. *Geochemistry, Geophysics, Geosystems*, 15(10): 4093-4115.
- Emerick, C.M., Duncan, R.A., 1982. Age progressive volcanism in the Comores Archipelago, western Indian Ocean and implications for Somali plate tectonics. *Earth and Planetary Science Letters*, 60(3): 415-428.
- Emerson, S., Hedges, J., 2008. Chemical Oceanography and the Marine Carbon Cycle.
- Etioppe, G., Sherwood Lollar, B., 2013. Abiotic methane on Earth. *Reviews of Geophysics*, 51(2): 276-299.
- Famin, V., Michon, L., Bourhane, A., 2020. The Comoros archipelago: a right-lateral transform boundary between the Somalia and Lwandle plates. *Tectonophysics*, 789: 228539.
- Feuillet, N., 2019. MAYOBS1 cruise, RV Marion Dufresne.
- Feuillet, N. et al., 2021. Birth of a large volcanic edifice offshore Mayotte via lithosphere-scale dyke intrusion. *Nature Geoscience*, 14: 787-795.
- Feuillet, N., Jorry, S., Rinnert, E., Thion, I., Fouquet, Y., 2019. MAYOBS cruises, RV Marion Dufresne.
- Fiebig, J. et al., 2004. Chemical and isotopic equilibrium between CO<sub>2</sub> and CH<sub>4</sub> in fumarolic gas discharges: Generation of CH<sub>4</sub> in arc magmatic-hydrothermal systems 1 Associate editor: M. Kusakabe. *Geochimica et Cosmochimica Acta*, 68(10): 2321-2334.
- Fouquet, Y., Feuillet, N., 2019. MAYOBS4 cruise, RV Marion Dufresne.
- Gamo, T. et al., 2001. Chemical characteristics of newly discovered black smoker fluids and associated hydrothermal plumes at the Rodriguez Triple Junction, Central Indian Ridge. *Earth and Planetary Science Letters*, 193(3): 371-379.
- Geo-Ocean (Ifremer), 2022. Bathymétrie - Mayotte (synthèse, 2021).
- Giggenbach, W.F., 1996. Chemical Composition of Volcanic Gases. In: Scarpa, R., Tilling, R.I. (Eds.), *Monitoring and Mitigation of Volcano Hazards*. Springer Berlin Heidelberg, Berlin, Heidelberg, pp. 221-256.
- Giggenbach, W.F., Sano, Y., Wakita, H., 1993. Isotopic composition of helium, and CO<sub>2</sub> and CH<sub>4</sub> contents in gases produced along the New Zealand part of a convergent plate boundary. *Geochimica et Cosmochimica Acta*, 57(14): 3427-3455.
- Glazer, B.T., Rouxel, O.J., 2009. Redox Speciation and Distribution within Diverse Iron-dominated Microbial Habitats at Loihi Seamount. *Geomicrobiology Journal*, 26(8): 606-622.

- Hekinian, R., Chaigneau, M., Cheminee, J.L., 1973. Popping Rocks and Lava Tubes from the Mid-Atlantic Rift Valley at 36° N. *Nature*, 245(5425): 371-373.
- Hilton, D.R., 1996. The helium and carbon isotope systematics of a continental geothermal system: results from monitoring studies at Long Valley caldera (California, U.S.A.). *Chemical Geology*, 127(4): 269-295.
- Hilton, D.R., Hammerschmidt, K., Teufel, S., Friedrichsen, H., 1993. Helium isotope characteristics of Andean geothermal fluids and lavas. *Earth and Planetary Science Letters*, 120(3-4): 265-282.
- Hilton, D.R., McMurtry, G.M., Goff, F., 1998. Large variations in vent fluid CO<sub>2</sub>/3He ratios signal rapid changes in magma chemistry at Loihi seamount, Hawaii. *Nature*, 396(6709): 359-362.
- Jansson, C., Northen, T., 2010. Calcifying cyanobacteria—the potential of biomineralization for carbon capture and storage. *Current Opinion in Biotechnology*, 21(3): 365-371.
- Jenkins, W.J. et al., 2019. A comprehensive global oceanic dataset of helium isotope and tritium measurements. *Earth System Science Data*, 11(7): 441-454.
- Jorry, S., 2019. MAYOBS2 cruise, RV Marion Dufresne.
- Kawagucci, S. et al., 2008. Methane, manganese, and helium-3 in newly discovered hydrothermal plumes over the Central Indian Ridge, 18°-20°S. *Geochemistry, Geophysics, Geosystems*, 9(10).
- Klein, F., Tarnas, J.D., Bach, W., 2020. Aqueous Sources of Molecular Hydrogen on Earth. *Elements*, 16(1): 19-24.
- Lappan, R. et al., 2023. Molecular hydrogen in seawater supports growth of diverse marine bacteria. *Nature Microbiology*, 8(4): 581-595.
- Lavayssière, A. et al., 2022. A new 1D velocity model and absolute locations image the Mayotte seismo-volcanic region. *Journal of Volcanology and Geothermal Research*, 421: 107440.
- Lemoine, A. et al., 2020. The 2018–2019 seismo-volcanic crisis east of Mayotte, Comoros islands: seismicity and ground deformation markers of an exceptional submarine eruption. *Geophysical Journal International*, 223(1): 22-44.
- Liu, B., Six, K.D., Ilyina, T., 2021. Incorporating the stable carbon isotope <sup>13</sup>C in the ocean biogeochemical component of the Max Planck Institute Earth System Model. *Biogeosciences*, 18(14): 4389-4429.
- Liuzzo, M. et al., 2021. Gas Geochemistry at Grande Comore and Mayotte Volcanic Islands (Comoros Archipelago), Indian Ocean. *Geochemistry, Geophysics, Geosystems*, 22(8).
- Lupton, J. et al., 2006. Submarine venting of liquid carbon dioxide on a Mariana Arc volcano. *Geochemistry, Geophysics, Geosystems*, 7(8).
- Lupton, J. et al., 2008. Venting of a separate CO<sub>2</sub>-rich gas phase from submarine arc volcanoes: Examples from the Mariana and Tonga-Kermadec arcs. *Journal of Geophysical Research: Solid Earth*, 113(B8).
- Lupton, J.E., Baker, E.T., Massoth, G.J., 1999. Helium, heat, and the generation of hydrothermal event plumes at mid-ocean ridges. *Earth and Planetary Science Letters*, 171(3): 343-350.

- Manoux, M. et al., 2023. Impact of volcanism on sedimentary diagenesis, Session: 13dO1 - Hydrothermal vents from discharge to biogeochemical impacts, Goldschmidt Conference: Lyon France 9-14 July 2023.
- Marty, B., Jambon, A., 1987. C/3He in volatile fluxes from the solid Earth: implications for carbon geodynamics. *Earth and Planetary Science Letters*, 83(1): 16-26.
- Marty, B., Jambon, A., Sano, Y., 1989. Helium isotopes and CO<sub>2</sub> in volcanic gases of Japan. *Chemical Geology*, 76(1-2): 25-40.
- Marty, B., Meynier, V., Nicolini, E., Griesshaber, E., Toutain, J.P., 1993. Geochemistry of gas emanations: A case study of the Réunion Hot Spot, Indian Ocean. *Applied Geochemistry*, 8(2): 141-152.
- Masquelet, C. et al., 2022a. The East-Mayotte new volcano in the Comoros Archipelago: structure and timing of magmatic phases inferred from seismic reflection data. *Comptes Rendus. Géoscience*, 354(S2): 65-79.
- Masquelet, C. et al., 2022b. Structure of a new submarine volcano and magmatic phases to the East of Mayotte, in the Comoros Archipelago, Indian Ocean. EGU General Assembly 2022, Vienna, Austria, 23–27 May 2022, EGU22-10766.
- Mayotte Volcanological And Seismological Monitoring Network (REVOSIMA), Institut de physique du globe de Paris (IPGP), Bureau de recherches géologiques et minières (BRGM), Institut français de recherche pour l'exploitation de la mer (IFREMER), Centre national de la recherche scientifique (CNRS), 2021. Data collection of the Mayotte volcanological and seismological monitoring network (REVOSIMA).
- McCollom, T.M., 2013. Laboratory Simulations of Abiotic Hydrocarbon Formation in Earth's Deep Subsurface. *Reviews in Mineralogy and Geochemistry*, 75(1): 467-494.
- McCollom, T.M., 2016. Abiotic methane formation during experimental serpentinization of olivine. *Proceedings of the National Academy of Sciences*, 113(49): 13965-13970.
- McDermott, J.M., Seewald, J.S., German, C.R., Sylva, S.P., 2015. Pathways for abiotic organic synthesis at submarine hydrothermal fields. *Proceedings of the National Academy of Sciences*, 112(25): 7668-7672.
- McLaughlin-West, F.A. et al., 1999. Variations in hydrothermal methane and hydrogen concentrations following the 1998 eruption at Axial Volcano. *Geophysical Research Letters*, 26(23): 3453-3456.
- Métrich, N., Wallace, P.J., 2008. Volatile Abundances in Basaltic Magmas and Their Degassing Paths Tracked by Melt Inclusions. *Reviews in Mineralogy and Geochemistry*, 69(1): 363-402.
- Michel, A.P.M., Wankel, S.D., Kapit, J., Sandwith, Z., Girguis, P.R., 2018. In situ carbon isotopic exploration of an active submarine volcano. *Deep Sea Research Part II: Topical Studies in Oceanography*, 150: 57-66.
- Michon, L., 2016. The Volcanism of the Comoros Archipelago Integrated at a Regional Scale. Springer Berlin Heidelberg, pp. 333-344.
- Milesi, V.P. et al., 2020. Early Diagenesis of Lacustrine Carbonates in Volcanic Settings: The Role of Magmatic CO<sub>2</sub> (Lake Dziani Dzaha, Mayotte, Indian Ocean). *ACS Earth and Space Chemistry*, 4(3): 363-378.

- Milkov, A.V., Etiope, G., 2018. Revised genetic diagrams for natural gases based on a global dataset of >20,000 samples. *Organic Geochemistry*, 125: 109-120.
- Nougier, J., Cantagrel, J.M., Karche, J.P., 1986. The Comores archipelago in the western Indian Ocean: volcanology, geochronology and geodynamic setting. *Journal of African Earth Sciences* (1983), 5(2): 135-145.
- Pegler, S.S., Ferguson, D.J., 2021. Rapid heat discharge during deep-sea eruptions generates megaplumes and disperses tephra. *Nature Communications*, 12(1).
- Pelleter, A.-A. et al., 2014. Melilite-bearing lavas in Mayotte (France): An insight into the mantle source below the Comores. *Lithos*, 208-209: 281-297.
- Perfit, M.R. et al., 2003. Interaction of sea water and lava during submarine eruptions at mid-ocean ridges. *Nature*, 426(6962): 62-65.
- Pörtner, H.-O. et al., 2022. IPCC, 2022, *Climate Change 2022: Impacts, Adaptation and Vulnerability Working Group II Contribution to the Sixth Assessment Report of the Intergovernmental Panel on Climate Change*, Cambridge University Press, Cambridge, UK and New York, NY, USA.
- Raynaud, D. et al., 1993. The Ice Record of Greenhouse Gases. *Science*, 259(5097): 926-934.
- Resing, J.A. et al., 2009. Chemistry of hydrothermal plumes above submarine volcanoes of the Mariana Arc. *Geochemistry, Geophysics, Geosystems*, 10(2).
- Resing, J.A. et al., 2007. Venting of Acid-Sulfate Fluids in a High-Sulfidation Setting at NW Rota-1 Submarine Volcano on the Mariana Arc. *Economic Geology*, 102(6): 1047-1061.
- Resing, J.A., Lupton, J.E., Feely, R.A., Lilley, M.D., 2004. CO<sub>2</sub> and <sup>3</sup>He in hydrothermal plumes: implications for mid-ocean ridge CO<sub>2</sub> flux. *Earth and Planetary Science Letters*, 226(3): 449-464.
- Resing, J.A. et al., 2011. Active submarine eruption of boninite in the northeastern Lau Basin. *Nature Geoscience*, 4(11): 799-806.
- Resing, J.A. et al., 2015. Basin-scale transport of hydrothermal dissolved metals across the South Pacific Ocean. *Nature*, 523(7559): 200-U140.
- REVOSIMA, Février 2021. Bulletin n°27 du 1er au 28 février 2021 : Bulletin de l'activité sismo-volcanique à Mayotte.
- Rinnert, E., Thinon, I., Feuillet, N., 2020. MD 228 / MAYOBS15 cruise, RV Marion Dufresne.
- Rubin, K.H. et al., 2012. Volcanic Eruptions in the Deep Sea. *Oceanography*, 25(1): 142-157.
- Sano, Y., Fischer, T.P., 2013. The Analysis and Interpretation of Noble Gases in Modern Hydrothermal Systems. In: Burnard, P. (Ed.), *The Noble Gases as Geochemical Tracers*. Springer Berlin Heidelberg, Berlin, Heidelberg, pp. 249-317.
- Sano, Y., Marty, B., 1995. Origin of carbon in fumarolic gas from island arcs. *Chemical Geology*, 119(1): 265-274.
- Sansone, F.J., Resing, J.A., 1995. Hydrography and geochemistry of sea surface hydrothermal plumes resulting from Hawaiian coastal volcanism. *Journal of Geophysical Research*, 100(C7): 13555.

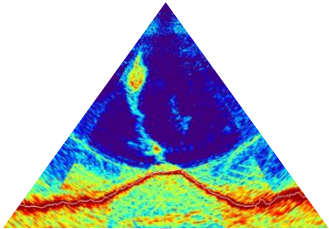
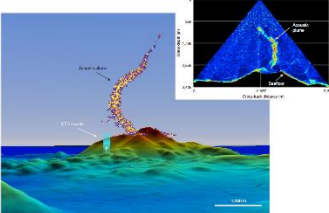
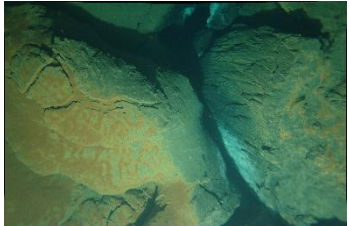


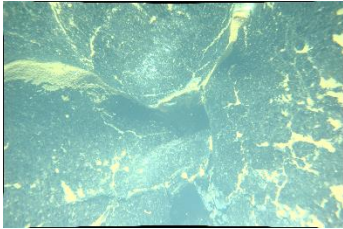
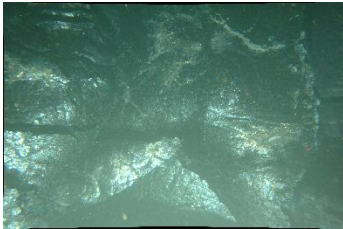

- Sansone, F.J. et al., 1991. Lava-seawater interactions at shallow-water submarine lava flows. *Geophysical Research Letters*, 18(9): 1731-1734.
- Santana-Casiano, J.M. et al., 2016. Significant discharge of CO<sub>2</sub> from hydrothermalism associated with the submarine volcano of El Hierro Island. *Scientific Reports*, 6(1): 25686.
- Schmittner, A. et al., 2013. Biology and air-sea gas exchange controls on the distribution of carbon isotope ratios ( $\delta^{13}\text{C}$ ) in the ocean. *Biogeosciences*, 10(9): 5793-5816.
- Span, R., Wagner, W., 1996. A New Equation of State for Carbon Dioxide Covering the Fluid Region from the Triple-Point Temperature to 1100 K at Pressures up to 800 MPa. *Journal of Physical and Chemical Reference Data*, 25(6): 1509-1596.
- Sültenfuß, J., 2016. Hints for sampling, Helis - helium isotopes studies Bremen.
- Sültenfuß, J., Roether, W., Rhein, M., 2009. The Bremen mass spectrometric facility for the measurement of helium isotopes, neon, and titanium in water. *Isotopes in Environmental and Health Studies*, 45(2): 83-95.
- Suzuki, A., 1998. Combined effects of photosynthesis and calcification on the partial pressure of carbon dioxide in seawater. *Journal of Oceanography*, 54(1): 1-7.
- Svensen, H. et al., 2004. Release of methane from a volcanic basin as a mechanism for initial Eocene global warming. *Nature*, 429(6991): 542-545.
- Symonds, R.B., Rose, W.I., Bluth, G.J.S., Gerlach, T.M., 1994. Volcanic-gas studies; methods, results, and applications. *Reviews in Mineralogy and Geochemistry*, 30(1): 1-66.
- Thinon, I., Rinnert, E., Feuillet, N., 2021. MAYOBS17 cruise, RV Pourquoi Pas ?
- Thordarson, T., Self, S., 1993. The Laki (Skaftár Fires) and Grímsvötn eruptions in 1783-1785. *Bulletin of Volcanology*, 55(4): 233-263.
- Truche, L., McCollom, T.M., Martinez, I., 2020. Hydrogen and Abiotic Hydrocarbons: Molecules that Change the World. *Elements*, 16(1): 13-18.
- Tsunogai, U. et al., 1994. Peculiar features of Suiyo Seamount hydrothermal fluids, Izu-Bonin Arc: Differences from subaerial volcanism. *Earth and Planetary Science Letters*, 126(4): 289-301.
- Tzevahirtzian, A., Zaragosi, S., Bachèlery, P., Biscara, L., Marchès, E., 2021. Submarine morphology of the Comoros volcanic archipelago. *Marine Geology*, 432: 106383.
- Wang, L., Jin, Z., Chen, X., Su, Y., Huang, X., 2023. The Origin and Occurrence of Natural Hydrogen. *Energies*, 16(5): 2400.
- Wang, Y. et al., 2020. Helium and carbon isotopic signatures of thermal spring gases in southeast Yunnan, China. *Journal of Volcanology and Geothermal Research*, 402: 106995.
- Weiss, R.F., 1971. Solubility of helium and neon in water and seawater. *Journal of Chemical & Engineering Data*, 16(2): 235-241.
- Weiss, R.F., 1974. Carbon dioxide in water and seawater: the solubility of a non-ideal gas. *Marine Chemistry*, 2(3): 203-215.

- Wen, H.-Y. et al., 2016. Helium and methane sources and fluxes of shallow submarine hydrothermal plumes near the Tokara Islands, Southern Japan. *Scientific Reports*, 6(1): 34126.
- White, J.D.L., Schipper, C.I., Kano, K., 2015. Chapter 31 - Submarine Explosive Eruptions. In: Sigurdsson, H. (Ed.), *The Encyclopedia of Volcanoes (Second Edition)*. Academic Press, Amsterdam, pp. 553-569.
- Worman, S.L., Pratson, L.F., Karson, J.A., Schlesinger, W.H., 2020. Abiotic hydrogen (H<sub>2</sub>) sources and sinks near the Mid-Ocean Ridge (MOR) with implications for the subseafloor biosphere. *Proceedings of the National Academy of Sciences of the United States of America*, 117(24): 13283-13293.
- Zhang, J., Quay, P.D., Wilbur, D.O., 1995. Carbon isotope fractionation during gas-water exchange and dissolution of CO<sub>2</sub>. *Geochimica et Cosmochimica Acta*, 59(1): 107-114.
- Zinke, J., Reijmer, J.J.G., Thomassin, B.A., 2003a. Systems tracts sedimentology in the lagoon of Mayotte associated with the Holocene transgression. *Sedimentary Geology*, 160(1): 57-79.
- Zinke, J., Reijmer, J.J.G., Thomassin, B.A., 2003b. Systems tracts sedimentology in the lagoon of Mayotte associated with the Holocene transgression. *Sedimentary Geology*, 160(1-3): 57-79.
- Zolotov, M.Y., Shock, E.L., 2000. A thermodynamic assessment of the potential synthesis of condensed hydrocarbons during cooling and dilution of volcanic gases. *Journal of Geophysical Research: Solid Earth*, 105(E1): 539-559.

## 12 TABLES

**Table 1.** Most striking features of the different lava flows and sampling sites, including site location, sampling date, visual observations from the submersible interactive camera system (SCAMPI, Ifremer) and main physicochemical characteristics.

Lava picture	CTD station & sampling date	Site	Activity	Suggested lava age	Visual	Observations	
						Turbidity, heat, density	Chemicals
 Ship echo sonder	MAY01-HY02 (16/05/2019)	Summit	Eruption		Acoustic plume of ~2 km high	Turbidity up to 0.8 NTU Presence of temperature and density anomaly	Maximum concentrations: $^3\text{He}_{\text{xs}} = \text{na}$ $\text{CO}_2 = 114.6 \mu\text{mol/L}$ $\text{CH}_4 = 224.8 \text{ nmol/L}$ $\text{H}_2 = 5992.9 \text{ nmol/L}$
 Figure from Feuillet et al., 2021	MAY01-HY03 (16/05/2019)	Northern flank	Eruption		1 km from the acoustic plume of ~2 km high	Turbidity up to 1.4 NTU from 2500 to 3000 m, and > 4.9 NTU for depths > 3000 m Presence of temperature and density anomaly	Maximum concentrations: $^3\text{He}_{\text{xs}} = \text{na}$ $\text{CO}_2 = 264.7 \mu\text{mol/L}$ $\text{CH}_4 = 830.5 \text{ nmol/L}$ $\text{H}_2 = 547.9 \text{ nmol/L}$
	MAY04-HYC4 (23/07/2019)	Northern flank	None	May 2019	Already emplaced lava flow, covered by a fine sediment deposit, with evidence for incipient fluid shimmering	Turbidity from 0.3 to 1.6 NTU Absence of temperature and density anomaly	Maximum concentrations: $^3\text{He}_{\text{xs}} = 11.33 \text{ fmol/L}$ $\text{CO}_2 = 32.7 \mu\text{mol/L}$ $\text{CH}_4 = 173.8 \text{ nmol/L}$ $\text{H}_2 = 1.3$

	MAY04-HY07 (22/07/2019) MAY04-HY09 (29/07/2019)	West lava flow	Recent	June 18th to July 30th 2019	More recent lava flow with yellowish staining and thin mats of probably microbial origin	Turbidity from 0.3 to 1.6 NTU Presence of temperature and density anomaly	Maximum concentrations: $^3\text{He}_{\text{xs}} = 15.44$ fmol/L $\text{CO}_2 = 105.9$ $\mu\text{mol/L}$ $\text{CH}_4 = 777.4$ nmol/L $\text{H}_2 = 39.3$ nmol/L
	MAY15-HY06 (17/10/2020)	Northwest lava flow	Very recent	May 11 <sup>th</sup> to October 11 <sup>th</sup> 2020	Very glossy black lava	Turbidity up to 0.6 NTU Presence of temperature and density anomaly	Maximum concentrations: $^3\text{He}_{\text{xs}} = 5.49$ fmol/L $\text{CO}_2 = 69.6$ $\mu\text{mol/L}$ $\text{CH}_4 = 204.4$ nmol/L $\text{H}_2 = 38.2$ nmol/L
	MAY15-HY08 (21/10/2020)	Northwest lava flow	Active flow	May 11 <sup>th</sup> to October 11 <sup>th</sup> 2020	Incandescent lava	Turbidity up to 0.6 NTU Presence of temperature and density anomaly	Maximum concentrations: $^3\text{He}_{\text{xs}} = 7.78$ fmol/L $\text{CO}_2 = 53.2$ $\mu\text{mol/L}$ $\text{CH}_4 = 283.6$ nmol/L $\text{H}_2 = 647.6$ nmol/L

**Table 2. Helium isotope concentrations, Neon concentrations and isotopic ratio calculations for seawater samples taken from July 2019 and October 2020 cruises at the northern volcano flank and above the various lava flows.**

Sample ID	Depth (m)	$^3\text{He}$ (mol/L)	$^4\text{He}$ (mol/L)	Ne (mol/L)	$^3\text{He}/^4\text{He}$	He/Ne $_{std}$	He/Ne $^4$	$^{20}\text{Ne}/\text{Ra}$	$^4\text{He}_{xs}$ (mol/L)	$^3\text{He}_{xs}$ (fmol/L)	$std\ ^3\text{He}_{xs}$	Rc/Ra $_{std}$	Rc/Ra	$\text{CO}_2/^3\text{He}$	
<b>MAY4-HY04 (July 2019, northern volcano flank)</b>															
MAY04-HY04-B01	3119.6	$1.39 \times 10^{-14}$	$3.34 \times 10^{-9}$	$8.23 \times 10^{-9}$	$4.17 \times 10^{-6}$	0.406	0.008	na	3.01	$1.46 \times 10^{-9}$	11.33	0.23	3.09	0.06	$2.16 \times 10^9$
MAY04-HY04-B07	2748.2	$1.17 \times 10^{-14}$	$3.10 \times 10^{-9}$	$8.18 \times 10^{-9}$	$3.77 \times 10^{-6}$	0.379	0.008	na	2.72	$1.22 \times 10^{-9}$	1.07	0.18	2.79	0.06	$2.70 \times 10^9$
MAY04-HY04-B14	2047.9	$2.91 \times 10^{-15}$	$1.99 \times 10^{-9}$	$7.99 \times 10^{-9}$	$1.46 \times 10^{-6}$	0.249	0.005	na	1.06	$1.5 \times 10^{-10}$	0.38	0.01	1.06	0.02	$9.09 \times 10^9$
MAY04-HY04-B15	1499.0	$2.93 \times 10^{-15}$	$1.99 \times 10^{-9}$	$7.79 \times 10^{-9}$	$1.47 \times 10^{-6}$	0.255	0.005	na	1.03	$2.03 \times 10^{-10}$	0.46	0.01	1.07	0.02	$9.49 \times 10^9$
<b>MAY4-HY07 (July 2019, Western recent lava flow)</b>															
MAY04-HY07-B03	2924.0	$1.80 \times 10^{-14}$	$3.74 \times 10^{-9}$	$8.16 \times 10^{-9}$	$4.82 \times 10^{-6}$	0.458	0.009	na	3.48	$1.87 \times 10^{-9}$	15.44	0.31	3.56	0.07	$3.66 \times 10^9$
<b>MAY15-HY06 (Oct. 2020, Northwest very recent lava flow)</b>															
MAY15-HY06-B01	3257.1	$8.13 \times 10^{-15}$	$2.38 \times 10^{-9}$	$8.32 \times 10^{-9}$	$3.42 \times 10^{-6}$	0.236	0.006	0.289	2.47	$4.67 \times 10^{-10}$	5.49	0.11	2.57	0.05	$6.76 \times 10^9$
MAY15-HY06-B02	3202.8	$6.87 \times 10^{-15}$	$2.26 \times 10^{-9}$	$8.30 \times 10^{-9}$	$3.04 \times 10^{-6}$	0.272	0.005	0.277	2.20	$3.46 \times 10^{-10}$	4.22	0.08	2.29	0.05	$7.96 \times 10^9$
MAY15-HY06-B04	3098.8	$6.94 \times 10^{-15}$	$2.25 \times 10^{-9}$	$8.29 \times 10^{-9}$	$3.08 \times 10^{-6}$	0.272	0.005	0.276	2.23	$3.44 \times 10^{-10}$	4.30	0.09	2.31	0.05	$8.10 \times 10^9$
MAY15-HY06-B08	2893.6	$1.08 \times 10^{-14}$	$2.60 \times 10^{-9}$	$8.22 \times 10^{-9}$	$4.16 \times 10^{-6}$	0.316	0.006	0.320	3.01	$7.09 \times 10^{-10}$	8.19	0.16	3.11	0.06	$5.73 \times 10^9$
MAY15-HY06-B11	2618.6	$6.31 \times 10^{-15}$	$2.19 \times 10^{-9}$	$8.27 \times 10^{-9}$	$2.89 \times 10^{-6}$	0.264	0.005	0.274	2.09	$2.83 \times 10^{-10}$	3.68	0.07	2.16	0.04	$9.11 \times 10^9$
MAY15-HY06-B14	2302.7	$4.79 \times 10^{-15}$	$2.09 \times 10^{-9}$	$8.33 \times 10^{-9}$	$2.29 \times 10^{-6}$	0.251	0.005	0.256	1.65	$1.68 \times 10^{-10}$	2.12	0.04	1.71	0.03	$1.20 \times 10^{10}$
MAY15-HY06-B16	1000.6	$2.87 \times 10^{-15}$	$1.85 \times 10^{-9}$	$7.90 \times 10^{-9}$	$1.55 \times 10^{-6}$	0.235	0.005	na	1.12	$7.56 \times 10^{-12}$	0.32	0.01	1.13	0.02	$2.15 \times 10^{10}$
<b>MAY15-HY08 (Oct. 2020, Northwest active lava flow)</b>															
MAY15-HY08-B02	3202.2	$3.94 \times 10^{-15}$	$2.03 \times 10^{-9}$	$8.44 \times 10^{-9}$	$1.94 \times 10^{-6}$	0.240	0.005	0.247	1.40	$7.70 \times 10^{-11}$	1.24	0.02	1.45	0.03	$9.85 \times 10^9$
MAY15-HY08-B04	3098.8	$9.90 \times 10^{-15}$	$2.57 \times 10^{-9}$	$8.23 \times 10^{-9}$	$3.85 \times 10^{-6}$	0.313	0.006	na	2.78	$6.84 \times 10^{-10}$	7.29	0.15	2.88	0.06	$4.61 \times 10^9$

MAY15-HY08-B07	2899.6	$1.05 \times 10^{-14}$	$2.54 \times 10^{-9}$	$8.39 \times 10^{-9}$	$4.11 \times 10^{-6}$	0.303	0.006	0.306	2.97	$6.07 \times 10^{-10}$	7.78	0.16	3.12	0.06	$4.78 \times 10^9$
MAY15-HY08-B09	2751.6	$7.23 \times 10^{-15}$	$2.28 \times 10^{-9}$	$8.21 \times 10^{-9}$	$3.17 \times 10^{-6}$	0.278	0.006	0.282	2.29	$3.97 \times 10^{-10}$	4.62	0.09	2.36	0.05	$6.48 \times 10^9$
MAY15-HY08-B11	2699.0	$7.63 \times 10^{-15}$	$2.30 \times 10^{-9}$	$8.20 \times 10^{-9}$	$3.31 \times 10^{-6}$	0.281	0.006	0.284	2.39	$4.21 \times 10^{-10}$	5.02	0.10	2.47	0.05	$6.18 \times 10^9$
MAY15-HY08-B14	2001.4	$3.69 \times 10^{-15}$	$1.97 \times 10^{-9}$	$8.37 \times 10^{-9}$	$1.87 \times 10^{-6}$	0.236	0.005	0.245	1.35	$3.09 \times 10^{-11}$	1.01	0.02	1.39	0.03	$1.29 \times 10^{10}$

*nd: not determined ; na: not analyzed.*

Journal Pre-proof

**Table 3. Summary of H<sub>2</sub>, CH<sub>4</sub>, CO<sub>2</sub>, TDMn, TDFe concentrations and pH, A<sub>T</sub>, ΣCO<sub>2</sub> and SiO<sub>2</sub> measured within the water column at the volcano summit, at the northern edifice flank and above the western and northwest lava flows, in May 2019, July 2019 and October 2020. These parameters are also presented for the both background hydrocasts used for background evaluation.**

Station	Bottle	Site	Activity	Sampling Date	Latitude	Longitude	Depth	CH <sub>4</sub>	H <sub>2</sub>	CO <sub>2</sub>	pH	ΔpH	A <sub>T</sub>	ΣCO <sub>2</sub>	Δ(ΣCO <sub>2</sub> )	SiO <sub>2</sub>	ΔSiO <sub>2</sub>	TdMn	TdFe
				(dd/mm/yyyy)				(nmol/L)	(nmol/L)	(μmol/L)				(μmol/L)	(μmol/L)	(μmol/L)	(μmol/L)	(nmol/L)	(nmol/L)
<b>MAYOBS01 cruise (May 2019), ongoing eruption</b>																			
MAY01-HY02	B01	Summit	Eruption	16/05/2019	-12.908872	45.71182	2717.0	224.8	39.2	716.5	7.16	-0.5	2501	2304	174.3	166.6	19.5	89.2	1841.8
MAY01-HY02	B02	Summit	Eruption	16/05/2019	-12.908831	45.71198	2640.3	56.6	11.1	147	7.47	-0.2	2701	2488	361.1	158.8	13.3	37.5	606.8
MAY01-HY02	B03	Summit	Eruption	16/05/2019	-12.908838	45.71196	2589.8	25.7	870.2	63.7	7.51	-0.2	2527	2379	253.9	156.5	12.1	60.6	1500.7
MAY01-HY02	B04	Summit	Eruption	16/05/2019	-12.90882	45.71198	2565.8	12.5	11.1	147	7.5	-0.2	2636	2423	298.8	154.3	10.5	23.2	306.1
MAY01-HY02	B05	Summit	Eruption	16/05/2019	-12.908835	45.71198	2490.4	11.9	111.7	114.6	7.45	-0.3	2527	2359	238.6	153.6	12.0	19.3	287.0
MAY01-HY02	B06	Summit	Eruption	16/05/2019	-12.90882	45.71198	2560.5	17.9	111.7	114.6	7.45	-0.3	2527	2359	238.6	153.6	12.0	19.3	287.0
MAY01-HY02	B07	Summit	Eruption	16/05/2019	-12.90883	45.71198	2510.7	27.8	2.8	104.2	7.52	-0.2	2504	2323	204.4	151.0	10.6	21.2	316.6
MAY01-HY02	B08	Summit	Eruption	16/05/2019	-12.90882	45.71198	2389.7	66.2	833.7	7.5	-0.2	2438	2291	173.1	155.8	15.8	60.0	647.3	
MAY01-HY02	B09	Summit	Eruption	16/05/2019	-12.90882	45.71198	2181.0	0.9	3351.5	43.6	7.65	-0.1	2436	2245	134.7	140.8	5.4	4.2	37.0
MAY01-HY02	B10	Summit	Eruption	16/05/2019	-12.90882	45.71198	1779.9	0.9	2287.8	60.6	7.63	-0.1	2435	2240	144.1	129.8	3.1	0.0	18.1
MAY01-HY02	B13	Summit	Eruption	16/05/2019	-12.90882	45.71198	1378.9	0.9	298.5	48.7	7.59	-0.2	2432	2249	167.6	120.1	2.1	3.0	55.7
MAY01-HY02	B14	Summit	Eruption	16/05/2019	-12.90882	45.71198	917.4	1.3	5992.9	36.9	7.62	-0.2	2439	2251	186.3	82.4	-25.6	2.2	22.5
MAY01-HY02	B15	Summit	Eruption	16/05/2019	-12.908805	45.712	485.3	1.9	1054.5	31.3	7.77	-0.1	2364	2143	93.9	13.3	-85.2	0.8	7.1
MAY01-HY02	B16	Summit	Eruption	16/05/2019	-12.90888	45.712	179.4	2.6	17.0	7.89	0.0	2378	2111	72.9	6.2	-85.7	0.7	8.2	
MAY01-HY03	B01	Northern flank	Eruption	16/05/2019	-12.90154	45.7149	3163.4	830.5	10.8	263.6	7.04	-0.6	2545	2434	288.2	162.7	5.8	560.2	10578.1
MAY01-HY03	B02	Northern flank	Eruption	16/05/2019	-12.90156	45.7149	3110.2	757.2	56.2	237.4	7.12	-0.5	2542	2397	253.1	164.2	8.5	312.2	8513.1
MAY01-HY03	B03	Northern flank	Eruption	16/05/2019	-12.90156	45.71494	3071.3	766.7	56.3	264.7	7.13	-0.5	2529	2409	266.5	162.3	7.5	309.1	8150.7
MAY01-HY03	B04	Northern flank	Eruption	16/05/2019	-12.90156	45.7149	3026.5	474.1	23.5	160.7	7.15	-0.5	2477	2349	208.2	162.1	8.3	288.7	7721.9

MAY01-HY03 B05	Northern flank	Eruption	16/05/2019	-12.90158	45.71494	2976.1	260.6	88.5	154.4	7.16-0.5	2467	2310	171.0			84.6	1775.0
MAY01-HY03 B06	Northern flank	Eruption	16/05/2019	-12.90156	45.71494	2891.0	441.8	21.9	264.4	7.16-0.5	2439	2324	188.1	160.7	9.8	142.1	3128.3
MAY01-HY03 B07	Northern flank	Eruption	16/05/2019	-12.90152	45.7149	2840.3	430.6	13.7	258.4	7.14-0.5	2495	2381	246.9	161.4	11.6	138.4	3136.4
MAY01-HY03 B08	Northern flank	Eruption	16/05/2019	-12.90156	45.71492	2720.9	280.3	20.3	202.2	7.16-0.5	2448	2324	194.2	160.5	13.3	120.5	2550.0
MAY01-HY03 B09	Northern flank	Eruption	16/05/2019	-12.90156	45.71492	2640.9	290.8	58.2	220.5	7.16-0.5	2444	2299	172.1	160.5	15.1	109.2	2495.6
MAY01-HY03 B10	Northern flank	Eruption	16/05/2019	-12.90156	45.71492	2600.4	198.9	34.4		7.16-0.5	2483	2301	175.5	157.4	12.8	85.5	1846.1
MAY01-HY03 B11	Northern flank	Eruption	16/05/2019	-12.90154	45.71492	2430.7	2.2	212.7	50.0	7.57-0.1	2429	2251	131.7	142.7	1.8	7.0	232.5
MAY01-HY03 B12	Northern flank	Eruption	16/05/2019	-12.90156	45.71492	2180.1	1.6	1.8	40.4	7.62-0.1	2455	2275	164.7	132.3	-3.1	2.8	74.2
MAY01-HY03 B13	Northern flank	Eruption	16/05/2019	-12.90156	45.7149	1929.6	2.6	519.8	42.1	7.78-0.2	2461	2278	176.7	128.9	-1.1	0.9	73.2
MAY01-HY03 B14	Northern flank	Eruption	16/05/2019	-12.90156	45.7149	1779.6	1.0	4.3	41.0	7.51-0.2	2442	2283	187.2	124.5	-2.3	0.0	79.5
MAY01-HY03 B15	Northern flank	Eruption	16/05/2019	-12.90156	45.71492	1614.7	3.7	547.9	4.5	7.56-0.2	2459	2237	147.1	120.4	-2.7	3.0	49.1
MAY01-HY03 B16	Northern flank	Eruption	16/05/2019	-12.90162	45.71488	1074.0	1.0	277.3	37.7	7.6-0.2	2410	2237	166.6	85.7	-25.7	3.3	56.9
<b>MAYOBS04 cruise (July 2019)</b>																	
MAY04-HY03 B01	Background	None	22/10/2019	-13.06938	45.65382	2498.7	0.6	0.0	20.0	7.790.15	2459.9	2251.8	93.9	159.5	-4.6	4.44	115.63
MAY04-HY03 B03	Background	None	22/10/2019	-13.06942	45.6388	2474.1	1.1	0.0	20.8	7.780.11	2381.2	2320.9	175.8	156.5	0.1	3.33	24.04
MAY04-HY03 B04	Background	None	22/10/2019	-13.06952	45.6376	2998.7	0.6		21.2	7.770.09	2346.8	2183.6	43.8	156.0	2.8	6.15	46.29
MAY04-HY03 B05	Background	None	22/10/2019	-13.06964	45.65374	2916.2	1.0	0.0	23.3	7.760.08	2380.3	2256.8	119.9	156.4	4.9	4.24	32.20
MAY04-HY03 B07	Background	None	22/10/2019	-13.06972	45.65356	2498.4	0.5	0.0	21.7	7.770.06	2383.2	2211.7	89.9	143.2	0.9	1.71	9.62
MAY04-HY03 B08	Background	None	22/10/2019	-13.06978	45.65352	1996.5	0.8	0.0	22.5	7.760.01	2363.5	2225.7	122.0	129.7	-1.7	8.10	126.34
MAY04-HY03 B09	Background	None	22/10/2019	-13.0698	45.65354	1948.5	0.6	0.0	23.2	7.74-0.01	2364.5	2196.6	94.7	128.0	-2.4	2.81	3.90
MAY04-HY03 B10	Background	None	22/10/2019	-13.06982	45.65348	1496.8	0.7	0.0	24.2	7.7-0.08	2362.6	2201.6	116.0	118.1	-2.5	4.66	318.16
MAY04-HY03 B12	Background	None	22/10/2019	-13.06978	45.6535	1347.2	0.5	0.0	23.9	7.7-0.09	2288.8	2015.2	-65.1	113.8	-3.5	2.50	9.98
MAY04-HY03 B14	Background	None	22/10/2019	-13.06982	45.65354	998.4	1.1	0.0	27.1	7.7-0.11	2335.0	2202.6	135.0	92.6	-17.1	1.83	13.91
MAY04-HY03 B16	Background	None	22/10/2019	-13.0698	45.6535	497.5	0.9	0.0	18.6	7.860.01	2324.2	2106.4	56.8	16.2	-82.6	1.83	20.61
MAY04-HY04 B01	Northern flank	None	23/10/2019	-12.90178	45.71518	3119.6	163.5	0.0	30.1	7.61-0.06	2372.0	2257.9	113.7	157.9	2.1	110.61	2956.48
MAY04-HY04 B03	Northern flank	None	23/10/2019	-12.90174	45.7152	3074.0	103.7	0.0	25.4	7.690.02	2360.0	2270.2	127.6	155.5	0.6	70.32	1729.92



MAY04-HY04 B04	Northern flank	None	23/10/2019	-12.90174	45.7152	2997.4	101.6	0.0	26.0	7.64-0.04	2451.0	2190.4	50.6	157.0	3.8	64.89	1599.10
MAY04-HY04 B05	Northern flank	None	23/10/2019	-12.90172	45.71522	2949.5	146.9	0.0	30.2	7.57-0.11	2438.0	2350.0	211.9	158.5	6.3	92.29	2484.55
MAY04-HY04 B06	Northern flank	None	23/10/2019	-12.90176	45.71514	2798.8	130.2	0.0	32.2	7.55-0.14	2394.0	2309.0	176.4	155.1	6.2	63.71	1248.33
MAY04-HY04 B07	Northern flank	None	23/10/2019	-12.90174	45.71514	2748.2	92.0	0.0	31.5	7.57-0.12	2445.0	2371.5	240.7	154.9	7.1	49.48	956.23
MAY04-HY04 B09	Northern flank	None	23/10/2019	-12.90174	45.71516	2598.2	78.5	0.0	29.3	7.66-0.04	2413.0	2269.1	143.8	151.2	6.7	35.96	635.77
MAY04-HY04 B10	Northern flank	None	23/10/2019	-12.90172	45.71518	2495.5	27.5	0.0	27.4	7.69-0.02	2392.0	2265.1	143.4	147.2	4.9	19.76	311.75
MAY04-HY04 B11	Northern flank	None	23/10/2019	-12.90174	45.71516	2248.3	173.8	0.0	32.7	7.59-0.14	2401.0	2242.5	129.8	145.3	8.4	58.83	1032.58
MAY04-HY04 B13	Northern flank	None	23/10/2019	-12.90174	45.71518	2121.7	1.9	0.0	30.4	7.76-0.02	2366.0	2203.7	95.5	133.6	-0.5	1.92	33.36
MAY04-HY04 B14	Northern flank	None	23/10/2019	-12.90174	45.71518	2047.9	45.1	1.3	26.4	7.73-0.01	2388.0	2265.1	159.5	135.7	3.1	15.92	222.88
MAY04-HY04 B15	Northern flank	None	23/10/2019	-12.90174	45.71518	1499.0	0.8	0.0	27.8	7.71-0.05	2370.0	2235.4	149.7	118.2	-2.4	5.53	25.26
MAY04-HY07 B03	West lava flow	Recent	27/07/2019	-12.91196	45.68738	2924.0	530.4	26.0	36.0	7.49-0.19	2490.6	2290.7	153.5	163.7	12.1	153.81	2097.72
MAY04-HY07 B04	West lava flow	Recent	27/07/2019	-12.91196	45.68736	2848.4	543.1	27.4	94.9	7.47-0.22	2453.5	2225.2	90.8	162.6	12.6	139.67	1870.03
MAY04-HY07 B05	West lava flow	Recent	27/07/2019	-12.91196	45.68738	2748.2	297.5	15.4	34.4	7.58-0.11	2460.7	2238.7	107.9	155.2	7.4	83.09	1186.34
MAY04-HY07 B06	West lava flow	Recent	27/07/2019	-12.91196	45.68736	2746.8	513.0	66.7	66.7	7.46-0.23	2491.6	2314.6	183.8	160.9	13.1	137.59	1856.08
MAY04-HY07 B08	West lava flow	Recent	27/07/2019	-12.91202	45.67362	2498.9	13.7	0.0	28.3	7.72-0.01	2428.9	2142.1	20.3	147.5	5.1	18.70	275.57
MAY04-HY07 B09	West lava flow	Recent	27/07/2019	-12.912	45.6736	2471.4	11.6	0.0	27.9	7.7-0.01	2442.2	2235.6	114.8	146.8	5.0	21.91	334.12
MAY04-HY07 B10	West lava flow	Recent	27/07/2019	-12.912	45.68736	2313.6	112.4	0.0	31.7	7.66-0.06	2429.9	2253.3	138.2	144.8	6.5	69.56	1295.62
MAY04-HY07 B12	West lava flow	Recent	27/07/2019	-12.912	45.68734	1997.6	1.1	0.0	25.9	7.76-0.01	2454.6	2267.8	164.1	128.4	-3.0	1.28	25.99
MAY04-HY07 B13	West lava flow	Recent	27/07/2019	-12.912	45.68732	1497.7	1.9	0.0	26.4	7.74-0.04	2352.8	2169.1	83.4	117.5	-3.1	15.45	38.75
MAY04-HY07 B14	West lava flow	Recent	27/07/2019	-12.91202	45.68732	967.5	1.1	0.0	26.6	7.73-0.09	2401.1	2247.0	180.5	82.7	-26.3	1.81	66.60
MAY04-HY07 B15	West lava flow	Recent	27/07/2019	-12.91196	45.6873	572.2	1.5	0.0	21.5	7.86-0.02	2343.5	2179.5	127.2	23.7	-76.8	38.92	723.30
MAY04-HY09 B01	West lava flow	Recent	29/07/2019	-12.9183	45.69218	3200.4	726.6	30.0	105.9	7.23-0.43	2448.7	1875.2	-271.9	165.0	7.4	237.37	4244.69
MAY04-HY09 B03	West lava flow	Recent	29/07/2019	-12.9183	45.69218	3154.5	777.4	39.3	101.8	7.16-0.51	2461.7	2155.5	10.0	167.0	10.4	268.03	4472.61
MAY04-HY09 B04	West lava flow	Recent	29/07/2019	-12.91828	45.69218	3112.7	648.6	3.7	50.9	7.56-0.11	2434.8	2180.4	36.5	162.8	7.0	189.82	3682.72
MAY04-HY09 B05	West lava flow	Recent	29/07/2019	-12.9183	45.69218	2978.1	645.2	4.9	53.6	7.43-0.25	2348.3	2127.6	-11.5	164.0	11.2	193.67	3222.76
MAY04-HY09 B06	West lava flow	Recent	29/07/2019	-12.91828	45.6922	2864.9	511.8	11.9	51.5	7.49-0.20	2357.2	2218.3	83.3	162.5	12.2	144.78	2420.97

MAY04-HY09 B07	West lava flow	Recent	29/07/2019	-12.9183	45.69222	2700.4	218.3	1.8	44.6	7.54-0.16	2369.2	2207.3	78.3	153.6	6.8	64.05	1608.02	
MAY04-HY09 B09	West lava flow	Recent	29/07/2019	-12.9183	45.6922	2641.2	348.2	1.1	57.7	7.48-0.22	2389.1	2288.1	161.2	154.9	9.4	99.87	2379.11	
MAY04-HY09 B11	West lava flow	Recent	29/07/2019	-12.9183	45.6922	2478.0	9.5	0.0	34.5	7.7-0.01	2372.2	2219.3	98.3	147.9	6.0	31.12	561.85	
MAY04-HY09 B12	West lava flow	Recent	29/07/2019	-12.9183	45.6922	2348.1	90.7	0.0	40.0	7.68-0.04	2324.4	2152.5	36.1	144.3	5.2	33.68	681.86	
MAY04-HY09 B14	West lava flow	Recent	29/07/2019	-12.9183	45.69222	2199.9	1.1	0.0	25.0	7.8-0.07	2441.8	2236.3	125.3	134.5	-1.4	0.00	44.74	
MAY04-HY09 B15	West lava flow	Recent	29/07/2019	-12.9183	45.69222	992.8	1.0	0.0	27.7	7.73-0.09	2330.4	2179.4	112.0	90.9	-18.7	0.00	0.20	
MAY04-HY09 B16	West lava flow	Recent	29/07/2019	-12.91832	45.69222	460.4	1.9	0.0	18.8	7.91-0.06	2217.1	2009.9	-38.4	15.5	-82.6	0.00	27.57	
<b>MAYOBS15 cruise (October 2020)</b>																		
MAY15-HY06 B01	Northwest lava flow	Very recent	17/10/2020	-12.8616	45.6771	3257.1	124.8	9.0	55.0	7.76-0.1	2356.1	2083.8	-65.3	156.1	-2.8	78.71	1165.50	
MAY15-HY06 B02	Northwest lava flow	Very recent	17/10/2020	-12.8616	45.67712	3202.8	42.8	2.8	54.7	7.6-0.1	2387.8	2136.2	-11.0	154.0	-3.7	45.30	614.48	
MAY15-HY06 B04	Northwest lava flow	Very recent	17/10/2020	-12.86162	45.6771	3098.8	78.5	13.0	56.2	7.58-0.1	2366.7	2124.8	-18.7	155.4	-0.1	44.89	707.64	
MAY15-HY06 B06	Northwest lava flow	Very recent	17/10/2020	-12.8616	45.6771	3001.6	204.4	30.2	69.6	7.49-0.2	2390.7	2152.4	12.4	158.1	4.8	76.89	880.66	
MAY15-HY06 B08	Northwest lava flow	Very recent	17/10/2020	-12.8616	45.6771	2893.3	95.1	7.1	61.9	7.54-0.1	2377.2	2134.3	-1.7	153.8	2.8	58.75	657.89	
MAY15-HY06 B09	Northwest lava flow	Very recent	17/10/2020	-12.86162	45.6771	2796.8	47.5	0.0	58.5	7.59-0.1	2386.8	2143.8	11.3	150.8	1.9	34.07	501.63	
MAY15-HY06 B10	Northwest lava flow	Very recent	17/10/2020	-12.8616	45.6771	2762.0	12.3	1.5	55.7	7.62-0.1	2358.0	2153.3	22.0	146.9	-1.2	19.06	294.75	
MAY15-HY06 B11	Northwest lava flow	Very recent	17/10/2020	-12.86162	45.6771	2618.6	25.0	1.0	57.5	7.64-0.1	2363.8	2141.9	15.8	147.5	2.5	24.05	409.64	
MAY15-HY06 B12	Northwest lava flow	Very recent	17/10/2020	-12.8616	45.6771	2542.8	21.3	1.7	57.7	7.63-0.1	2361.9	2156.2	32.8	146.1	2.7	19.68	294.61	
MAY15-HY06 B13	Northwest lava flow	Very recent	17/10/2020	-12.8616	45.67712	2400.3	1.3	1.1	57.2	7.67-0.0	2357.1	2131.4	13.2	138.3	-1.9	5.11	115.23	
MAY15-HY06 B14	Northwest lava flow	Very recent	17/10/2020	-12.86158	45.67712	2302.7	0.7	0.0	57.6	7.65-0.1	2363.8	2142.9	28.1	135.7	-2.4	6.14	145.05	
MAY15-HY06 B16	Northwest lava flow	Very recent	17/10/2020	-12.86162	45.6771	1000.6	1.2	0.0	61.7	7.62-0.2	2279.3	2053.4	-14.4	82.1	-27.7	0.80	160.72	
MAY15-HY08 B01	Northwest lava flow	Active flow	21/10/2020	-12.87088	45.6855	3259.2	283.6	171.3	46.9	7.58-0.1	2451.6	2423.5	274.2	158.6	-0.3	117.26	1878.76	
MAY15-HY08 B02	Northwest lava flow	Active flow	21/10/2020	-12.87088	45.6855	3202.2	5.0	12.4	38.8	7.61-0.1	2393.4	2165.7	18.5	154.0	-3.7	10.91	194.94	
MAY15-HY08 B04	Northwest lava flow	Active flow	21/10/2020	-12.87086	45.6855	3098.8	44.5	14.1	45.7	7.57-0.1	2212.1	2202.1	58.7	156.2	0.8	49.67	600.08	
MAY15-HY08 B06	Northwest lava flow	Active flow	21/10/2020	-12.87088	45.6855	2999.9	131.3	308.2	45.5	7.61-0.1	2413.8	2166.7	26.8	157.8	4.5	55.13	673.76	
MAY15-HY08 B07	Northwest lava flow	Active flow	21/10/2020	-12.87088	45.6855	2899.6	122.4	290.8	50.0	7.58-0.1	2410.8	2203.1	66.8	157.0	5.9	61.99	682.35	
MAY15-HY08 B08	Northwest lava flow	Active flow	21/10/2020	-12.87088	45.6855	2827.7	107.3	525.4	48.3	7.7-0.0	2418.6	2184.9	51.2	156.1	6.6	49.56	570.35	

MAY15-HY08 B09	Northwest lava flow	Active flow	21/10/2020	-12.87088	45.6855	2751.6	110.6	537.9	46.9	7.63	-0.1	2404.1	2172.4	41.5	157.0	9.1	51.21	614.98
MAY15-HY08 B11	Northwest lava flow	Active flow	21/10/2020	-12.8709	45.68548	2699.0	140.6	647.6	47.1	7.67	0.0	2422.5	2173.4	44.3	158.2	11.5	54.13	666.90
MAY15-HY08 B12	Northwest lava flow	Active flow	21/10/2020	-12.8709	45.6855	2600.6	0.8	6.7	50.3	7.68	0.0	2393.4	2140.8	15.3	149.3	4.8	68.75	146.75
MAY15-HY08 B13	Northwest lava flow	Active flow	21/10/2020	-12.87088	45.6855	2499.2	2.3	6.8	49.2	7.66	-0.1	2410.8	2181.0	59.2	144.5	2.2	9.23	97.67
MAY15-HY08 B14	Northwest lava flow	Active flow	21/10/2020	-12.87086	45.6855	2001.4	0.6	2.5	47.7	7.76	0.0	2326.5	2112.0	8.2	127.4	-4.1	3.21	43.54
MAY15-HY08 B16	Northwest lava flow	Active flow	21/10/2020	-12.87088	45.6855	987.7	1.2	1.8	53.2	7.71	-0.1	2334.3	2124.5	57.2	83.5	-26.0		
MAY15-HY09 B01	Background	None	22/10/2020	-12.08746	46.0565	3507.0	0.6	0.0	44.4	7.61	0.0	2376.1	2179.9	21.7	156.8	-7.5	0.00	17.45
MAY15-HY09 B03	Background	None	22/10/2020	-12.08748	46.05648	3299.4	0.4	0.0	45.4	7.64	0.0	2417.1	2154.6	3.9	157.8	-2.0	4.51	43.77
MAY15-HY09 B04	Background	None	22/10/2020	-12.08746	46.0565	2992.2	0.4	0.0	46.6	7.64	0.0	2399.6	2079.8	-59.8	155.9	2.8	5.98	130.66
MAY15-HY09 B06	Background	None	22/10/2020	-12.08748	46.05648	2901.9	0.2	0.0	47.7	7.61	0.0	2394.7	2145.9	9.5	152.3	1.1	5.18	62.92
MAY15-HY09 B07	Background	None	22/10/2020	-12.08748	46.0565	2797.1	0.2	0.0	50.6	7.66	0.0	2408.3	2153.7	21.1	153.2	4.3	22.98	108.60
MAY15-HY09 B08	Background	None	22/10/2020	-12.08746	46.0565	2587.5	0.2	0.0	47.3	7.68	0.0	2443.4	2224.6	99.6	149.7	5.4	5.99	119.07
MAY15-HY09 B09	Background	None	22/10/2020	-12.0875	46.0565	2294.1	0.1	0.0	49.7	7.67	-0.1	2407.4	2155.6	41.2	141.1	3.2	1.74	15.64
MAY15-HY09 B11	Background	None	22/10/2020	-12.08748	46.05648	1585.5	0.7	0.0	53.9	7.65	-0.1	2363.5	2171.2	82.3	119.2	-3.3	0.22	14.08
MAY15-HY09 B12	Background	None	22/10/2020	-12.0875	46.0565	1000.1	1.4	0.0	56.6	7.64	-0.2	2352.8	2138.1	70.4	86.6	-23.1	15.86	188.82
MAY15-HY09 B14	Background	None	22/10/2020	-12.0875	46.0565	498.9	1.2	1.1	52.8	7.84	0.0	2313.9	2050.6	1.0	13.2	-85.7	7.34	50.05
MAY15-HY09 B15	Background	None	22/10/2020	-12.0875	46.0565	94.8	2.2	0.0	17.0	8.14	0.3	2310.0	1978.7	-56.3	1.5	-88.6	9.84	204.35

**Table 4. Concentrations of CH<sub>4</sub> and CO<sub>2</sub> and their isotopic carbon composition,  $\delta^{13}\text{C-CH}_4$  and  $\delta^{13}\text{C-CO}_2$ , in seawater samples taken above recent, very recent and active lava flows from July 2019 and October 2020 cruises.**

Sample ID	Depth (m)	CH <sub>4</sub> (nmol/L)	CO <sub>2</sub> ( $\mu\text{mol/L}$ )	$\delta^{13}\text{C-CH}_4$ (‰, vs. vPDB)	$\delta^{13}\text{C-CO}_2$ (‰, vs. vPDB)
<b>MAY4-HY07 (July 2019, Western recent lava flow)</b>					
MAY4-HY07-B3	2924.0	530.4	66.0	-34.8	na
MAY4-HY07-B6	2746.8	518.0	66.7	na	-0.6
<b>MAY15-HY06 (Oct. 2020, Northwest very recent lava flow)</b>					
MAY15-HY06-B1	3257.1	124.8	55.0	na	-0.5
MAY15-HY06-B2	3202.8	42.8	54.7	na	-1.1
<b>MAY15-HY08 (Oct. 2020, Northwest active lava flow)</b>					
MAY15-HY08-B1	3259.2	283.6	16.9	-34	-1.4
MAY15-HY08-B4	3098.8	44.5	45.7	na	-1.3
MAY15-HY08-B7	2899.6	122.4	50.0	na	-1.3

*na: not analyzed (due to low gas concentrations).  $\delta^{13}\text{C-CO}_2$  values are corrected for carbon isotope fractionation between  $\text{CO}_{2(\text{g})}$  and  $\text{CO}_{2(\text{aq})}$ , at 25°C and seawater salinity, following Eq. 4 from Assayag et al. (2006) and using fractionation factors from Zhang et al. (1995) and  $\text{CO}_2$  solubilities from Weiss (1974).*

### 13 FIGURE CAPTIONS

**Figure 1.** (A) Map of the site with reference CTD casts and 50m-resolution bathymetry using WGS 84 geodetic system (Geo-Ocean (Ifremer), 2022), (B) Bathymetry (30m-resolution) of the volcano edifice with CTD casts performed above the volcano and above lava flows, (C) 3D representation of the volcano edifice (vertical exaggeration x2).

**Figure 2.** Turbidity profiles determined by background evaluation, and measured for the studied hydrocasts from May 2019, July 2019 and October 2020 (MAYOBS1, MAYOBS4 and MAYOBS15 cruises, respectively). Please pay attention to the differences in NTU scales between the background profile and the others.

**Figure 3.** Depth profiles of  $^3\text{He}_{\text{xs}}$  concentration measured at the northern flank of the volcano and above the recent Western lava flow in July 2019 during MAYOBS4 cruise (in green), and above the North West very recent lava flow in October 2020 during MAYOBS15 cruise (in purple). The evaluated background for  $^3\text{He}_{\text{xs}}$  concentrations is represented by the bold line.

**Figure 4.** Depth profiles of studied dissolved gases at the eruption site during the May 2019 eruption (in orange) and two months later (in green). MAY01-HY02 cast (from May 2019) was performed at the volcano summit while MAY01-HY03 (from May 2019) and MAY04-HY04 (from July 2019) were sampled at the northern flank of the volcano. (A<sub>1</sub>) H<sub>2</sub> profiles; (A<sub>2</sub>) Zoom in H<sub>2</sub> profiles for H<sub>2</sub> concentrations from 0 to 600 nmol/L; (B) CO<sub>2</sub> profiles; (C) CH<sub>4</sub> profiles. Evaluated background is represented by the bold line and the grey envelop.

**Figure 5.** Depth profiles of dissolved gases measured above recent (in green) and very recent lava flow (in purple). MAY04-HY07 (from July 2019) and MAY04-HY09 (from July 2019) casts were performed above the recent Western lava flow while MAY15-HY06 (from October 2020) was

sampled above the very recent lava flow from and MAY15-HY08 (from October 2020) above the incandescent lava flow both from the North West site. **(A<sub>1</sub>)** H<sub>2</sub> profiles; **(A<sub>2</sub>)** Zoom in H<sub>2</sub> profiles for H<sub>2</sub> concentrations from 0 to 60 nmol/L; **(B)** CO<sub>2</sub> profiles; **(C)** CH<sub>4</sub> profiles. Evaluated background is represented by the bold line and the grey envelop.

**Figure 6.** Depth profiles of **(A)** pH; **(B)** Total alkalinity; **(C)** Total CO<sub>2</sub>; **(D<sub>1</sub>)** SiO<sub>2</sub> and **(D<sub>2</sub>)** ΔSiO<sub>2</sub> that is the change in SiO<sub>2</sub> from the regional background. Seawater samples from all three cruises from May 2019 (MAYOBS1 in orange), July 2019 (MAYOBS4 in green) and October 2020 (MAYOBS15 in purple) are plotted. Background is represented by the bold line and the grey envelop, determined from two background hydrocasts.

**Figure 7.** Depth profiles of **(A)** Total Dissolvable Mn (TDMn) and **(B)** Total Dissolvable Fe (TDFe). **(C)** Plots of TDFe vs. TDMn. All hydrocasts performed during the three cruises are represented: May 2019 (MAYOBS1 in orange), July 2019 (MAYOBS4 in green), and October 2020 (MAYOBS15 in purple). **(C1)** shows the entire data set; **(C2)** focusses on smaller levels of TDFe and TDMn. Ratios of TDFe/TDMn evolve between 11 and 27 (in mol/mol). TDFe/TDMn ratios were determined for each cast: MAY01-HY02 (17.8, r<sup>2</sup>= 0.94); MAY01-HY03 (22.5, r<sup>2</sup>= 0.97); MAY04-HY04 (23.9, r<sup>2</sup>= 0.98); MAY04-HY07 (13.9, r<sup>2</sup>= 0.99); MAY04-HY09 (17.8, r<sup>2</sup>= 0.99); MAY15-HY06 (13.4, r<sup>2</sup>= 0.97); MAY15-HY08 (12.2, r<sup>2</sup>= 0.89).

**Figure 8.** Rc/Ra ratio versus Ne/He **(A)** and He/Ne **(B)** for seawater samples from July 2019 (MAYOBS4 in green) and October 2020 (MAYOBS15 in purple). ASW dot is the Air Saturated Water value. **(A)** The blue arrow shows helium enrichment due to air contamination, the green arrow would represent the addition of radiogenic <sup>4</sup>He, the gold arrow the addition of tritiogenic <sup>3</sup>He (from tritium radioactive decay). Our seawater samples are mainly driven by the addition of magmatic <sup>3</sup>He. **(B)** ASW, mantle and crust are isotopic ratios for corresponding end-members. ASW: Rc/Ra = 1,

$^4\text{He}/\text{Ne} = 0.226$  (Hilton, 1996; Weiss, 1971); upper mantle (MORB-like):  $\text{Rc}/\text{Ra} = 8 \pm 1.5$ ,  $^4\text{He}/\text{Ne} = 1000$  (Sano and Fischer, 2013); crust:  $\text{Rc}/\text{Ra} = 0.02$ ,  $^4\text{He}/\text{Ne} = 1000$  (Wang et al., 2020). Dashed plots are the calculated binary mixing curves between the different endmembers. The uncertainty on  $\text{Rc}/\text{Ra}$  and  $\text{He}/\text{Ne}$  measurements is lower the size of the symbols.

**Figure 9.** Composite representation of gas concentration profiles, water column physical parameters and bathymetry of the Fani Maoré Seamount during the May 2019 eruption (MAYOBS1 cruise). Profiles of  $\text{H}_2$ ,  $\text{CO}_2$  and  $\text{CH}_4$  were measured at the summit and above the northern flank of the volcano. Pure- $\text{CO}_2$  density changes with the water column depth at the volcano was calculated using Span and Wagner's equation of state (Span and Wagner, 1996). Standard-seawater density profile was calculated from CTD data recorded at both sites and Archer's thermodynamic model for NaCl (Archer, 1992). Temperature profile was extracted from CTD data recorded at both sites. 3D representation of the volcano edifice was made using 30m-resolution bathymetry (vertical exaggeration x2), with counter lines at 50m intervals (Geo-Ocean (Ifremer), 2022).

**Figure 10.** Plot of  $\Delta\Sigma\text{CO}_2$  vs.  $\Delta\text{pH}$  for all seawater samples taken during the three cruises: May 2019 (MAYOBS1 in orange), July 2019 (MAYOBS4 in green) and October 2020 (MAYOBS15 in purple).  $\Delta$  values are the change in  $\Sigma\text{CO}_2$  and pH from the regional background. The blue arrow shows the decrease in pH caused by mineral acidity addition ( $\text{H}^+$ ). The brown arrow represents the increase in pH due to carbonate alkalinity addition resulting from the rock weathering. The red dash line ( $-360 \mu\text{mol}/\text{L}$  per pH) shows the theoretical decrease in pH in the case of only  $\text{CO}_2$  is added. When both carbonate alkalinity and  $\text{CO}_2$  are added, pH decreases. (Theoretical trends from Resing et al. (2009)).

**Declaration of interests**

The authors declare that they have no known competing financial interests or personal relationships that could have appeared to influence the work reported in this paper.

The authors declare the following financial interests/personal relationships which may be considered as potential competing interests:

Journal Pre-proof



## Highlights

- Massive gases released in the water column during the eruption
- Emitted gases respond in an uncoupled way due to original settings of the volcano
- Strong water column acidification due to the release of CO<sub>2</sub>-rich fluids
- Water column enrichments in iron and manganese by fluid-rock interactions
- Helium isotope signatures show evidence of a change in the magma path

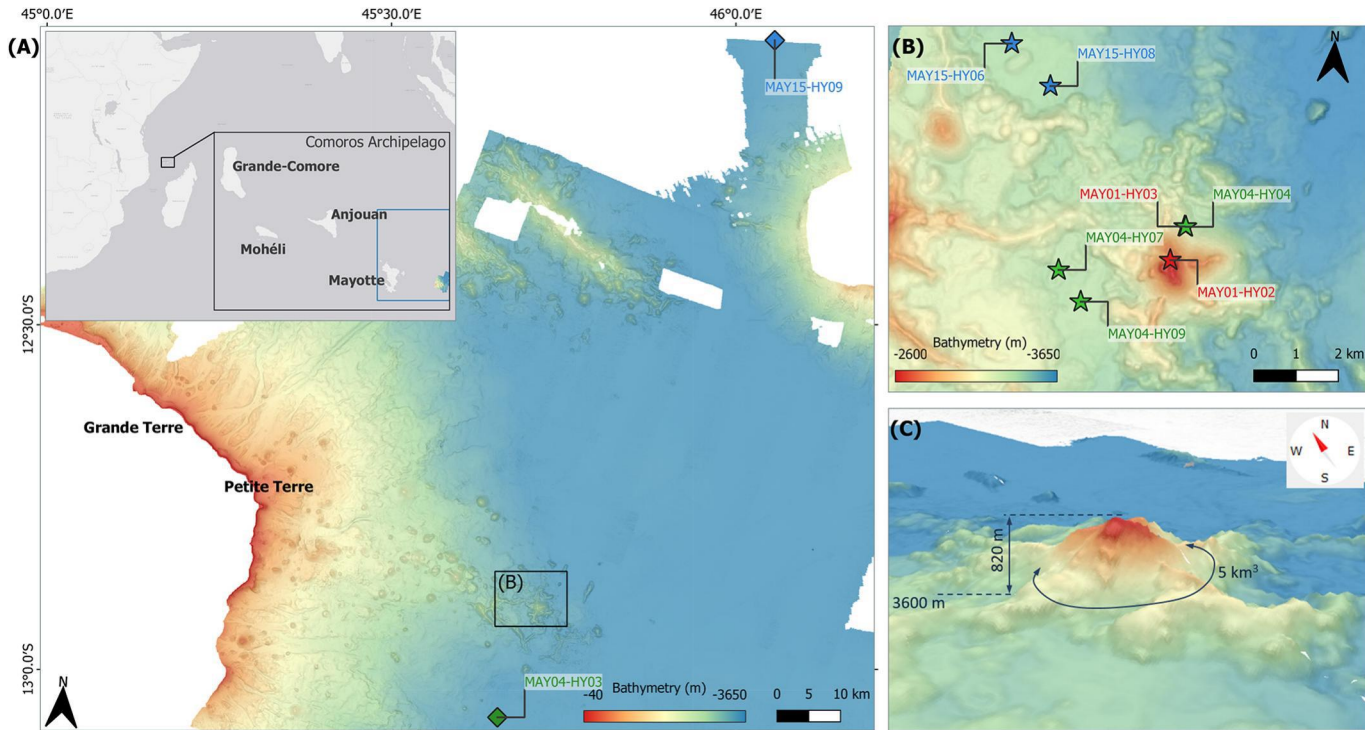


Figure 1

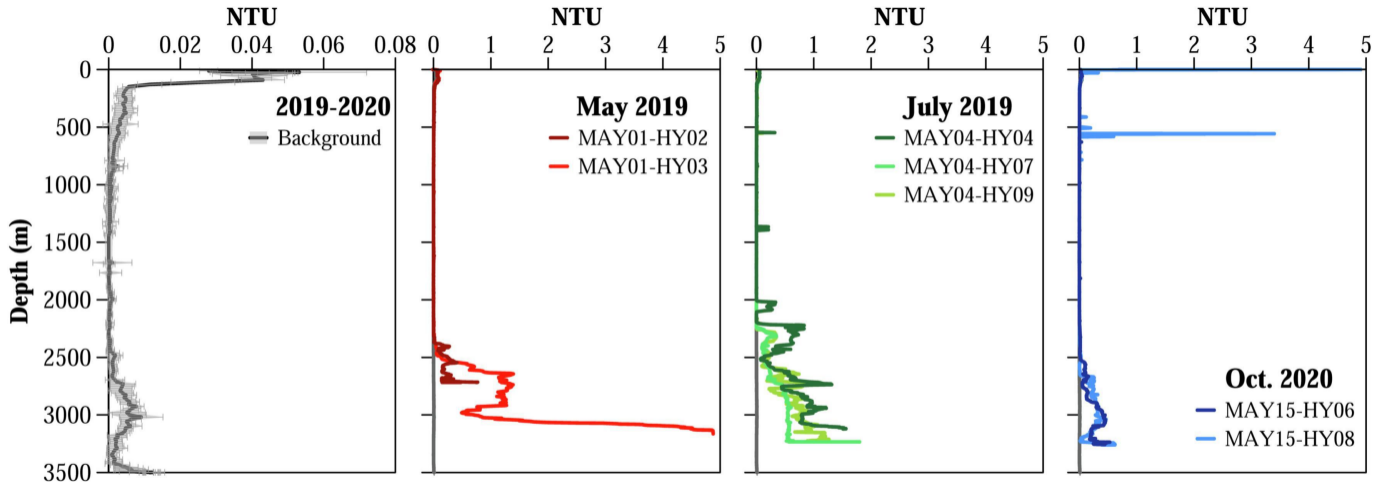
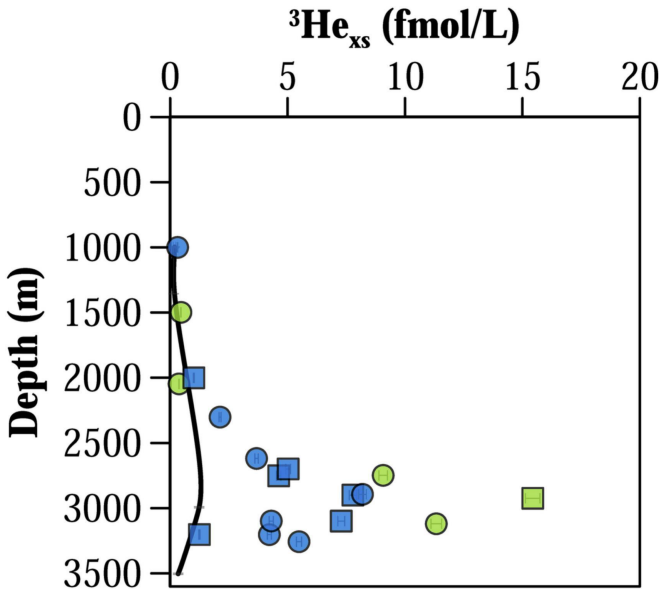


Figure 2



- Background
- MAY04-HY04 (July 19, flank)
- MAY04-HY07 (July 19, recent lava)
- MAY15-HY06 (Oct 20, very recent lava)
- MAY15-HY08 (Oct 20, incandescent lava)

Figure 3

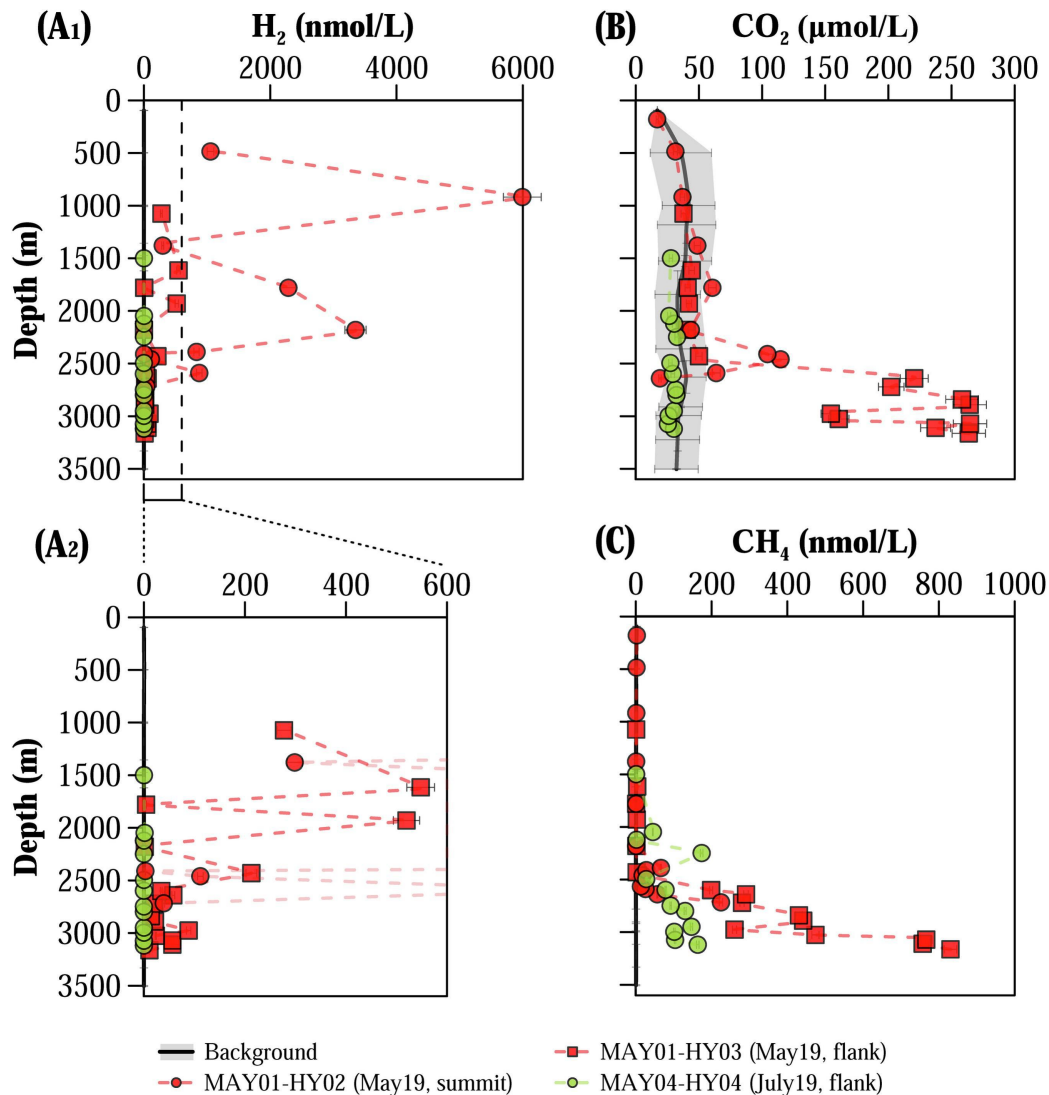


Figure 4

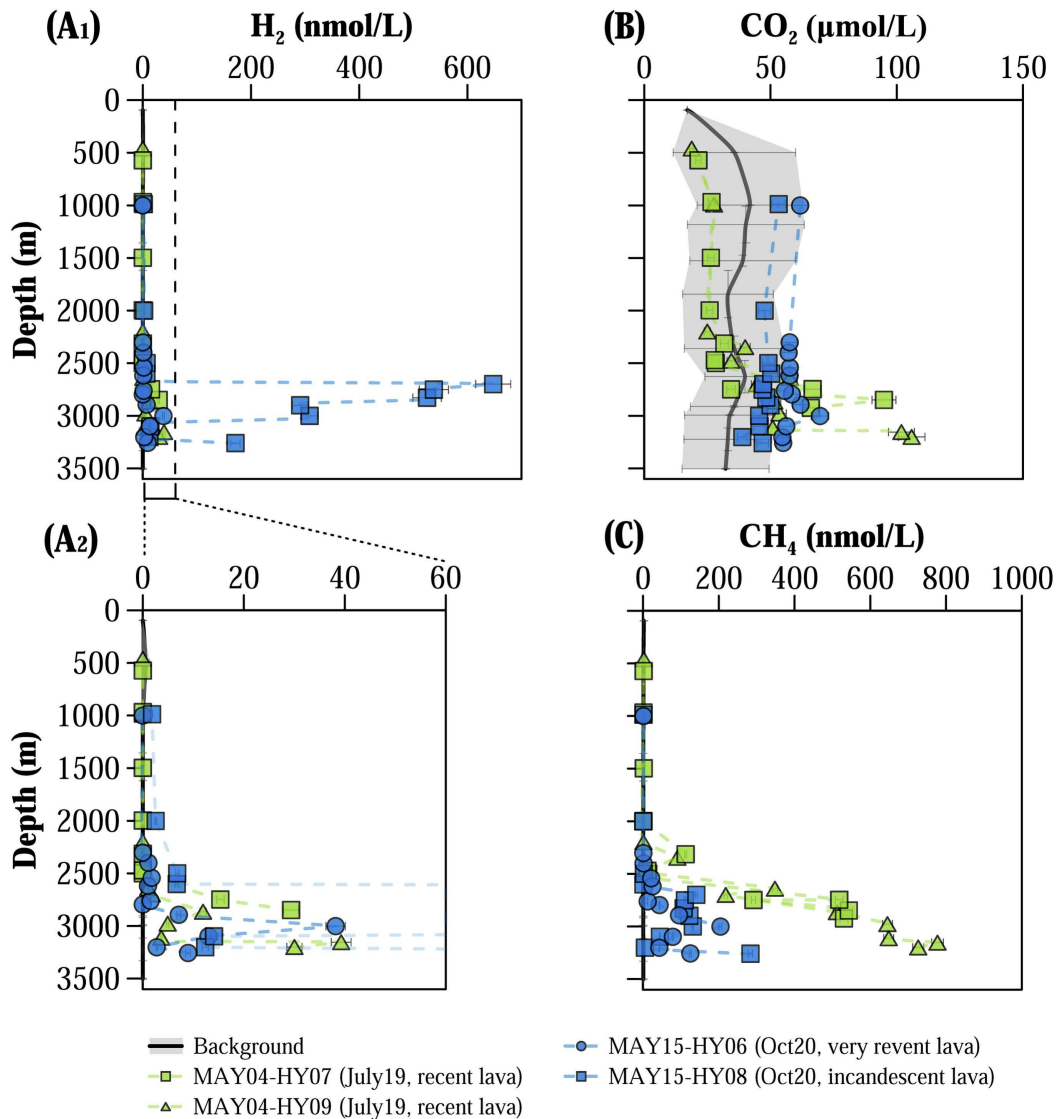


Figure 5

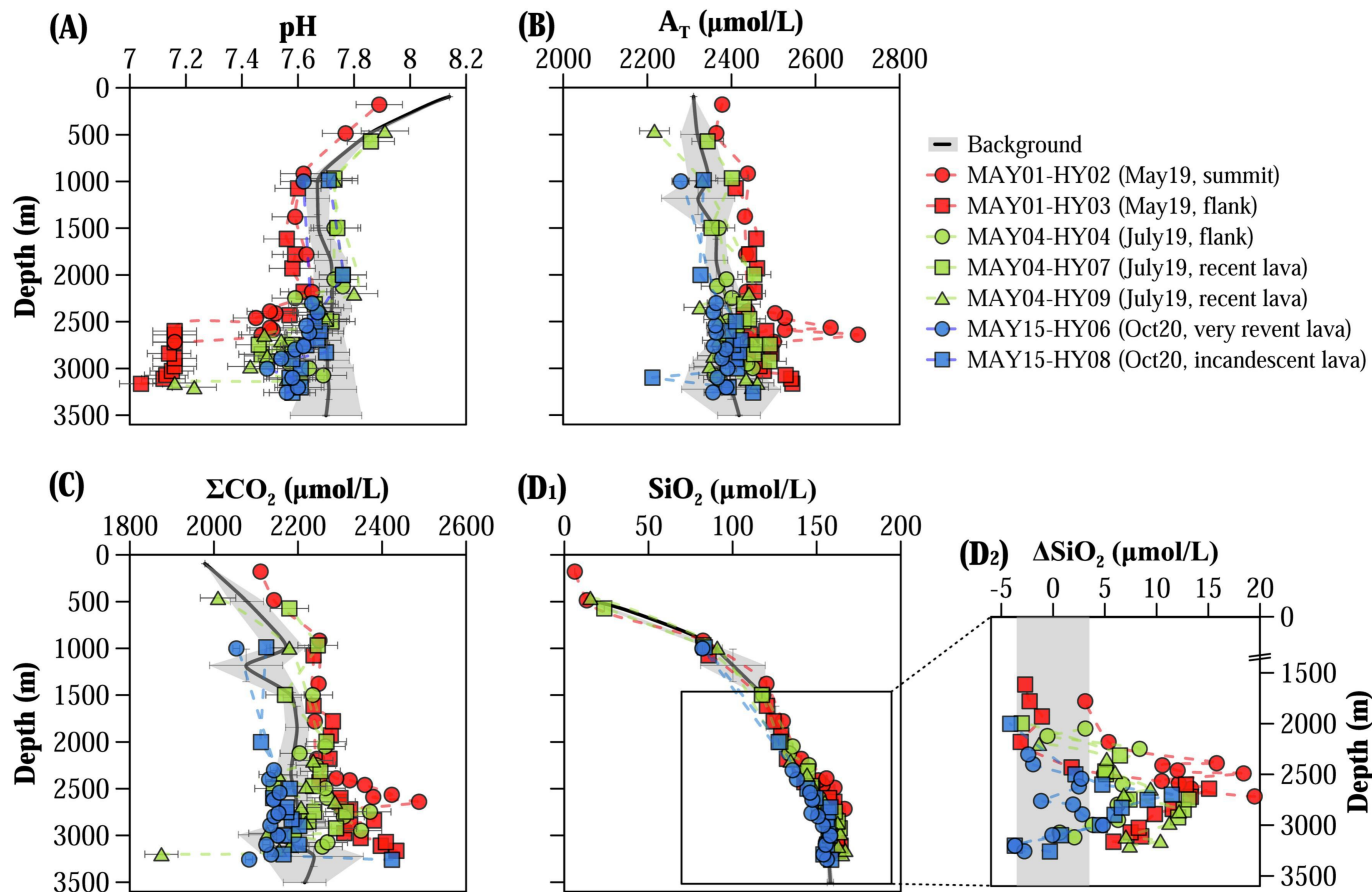


Figure 6

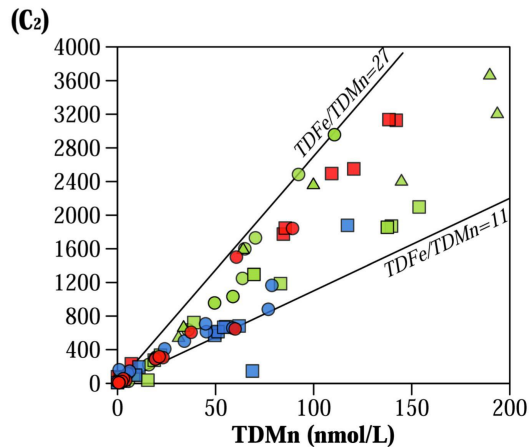
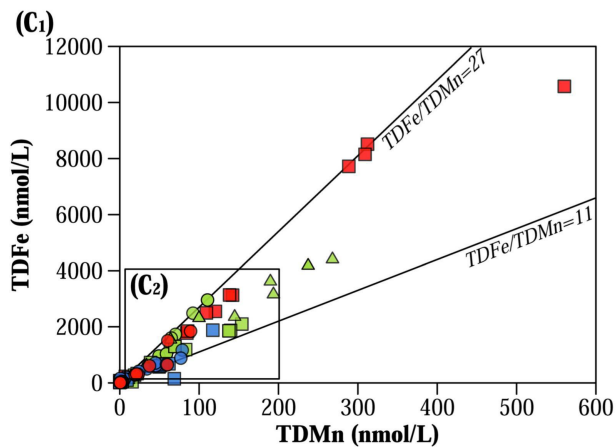
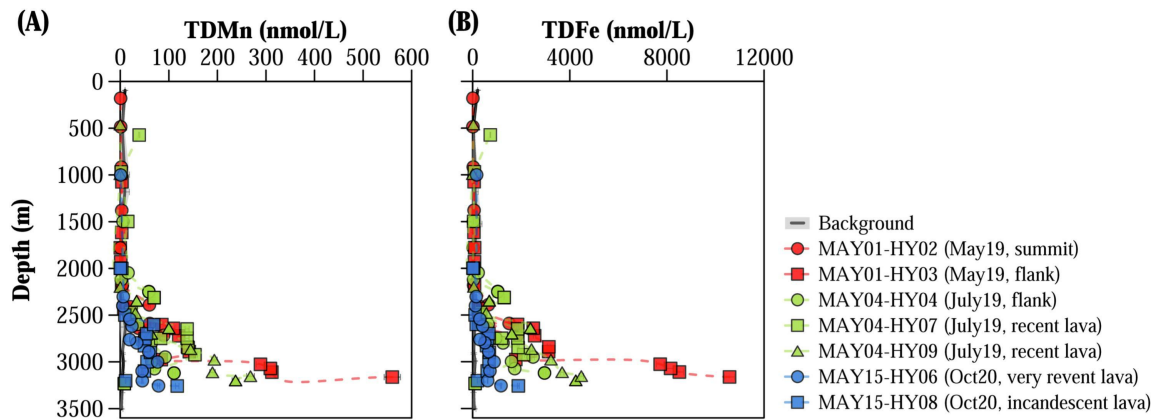
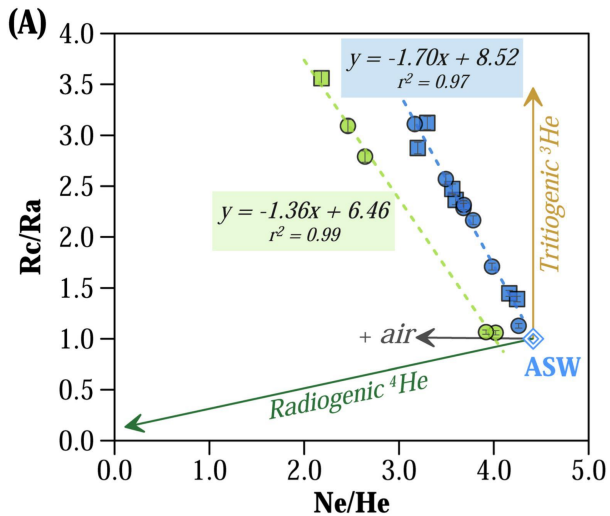
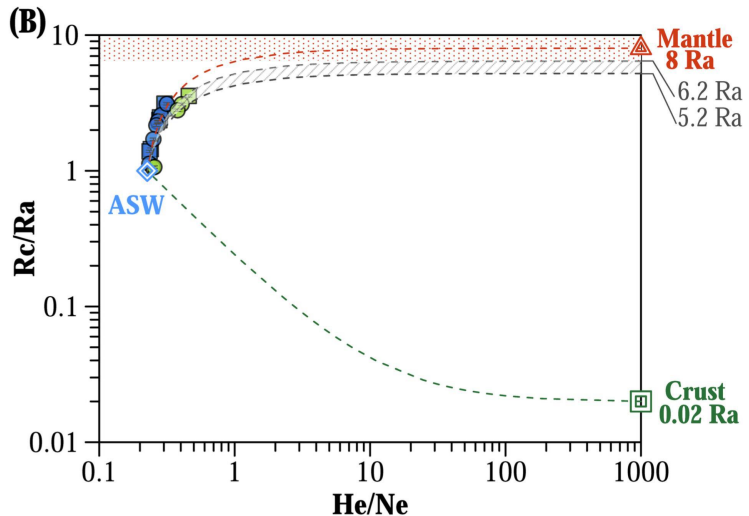


Figure 7





- MAY04-HY04 (July19, flank)
- MAY04-HY07 (July19, recent lava)



- MAY15-HY06 (Oct20, very revent lava)
- MAY15-HY08 (Oct20, incandescent lava)

Figure 8

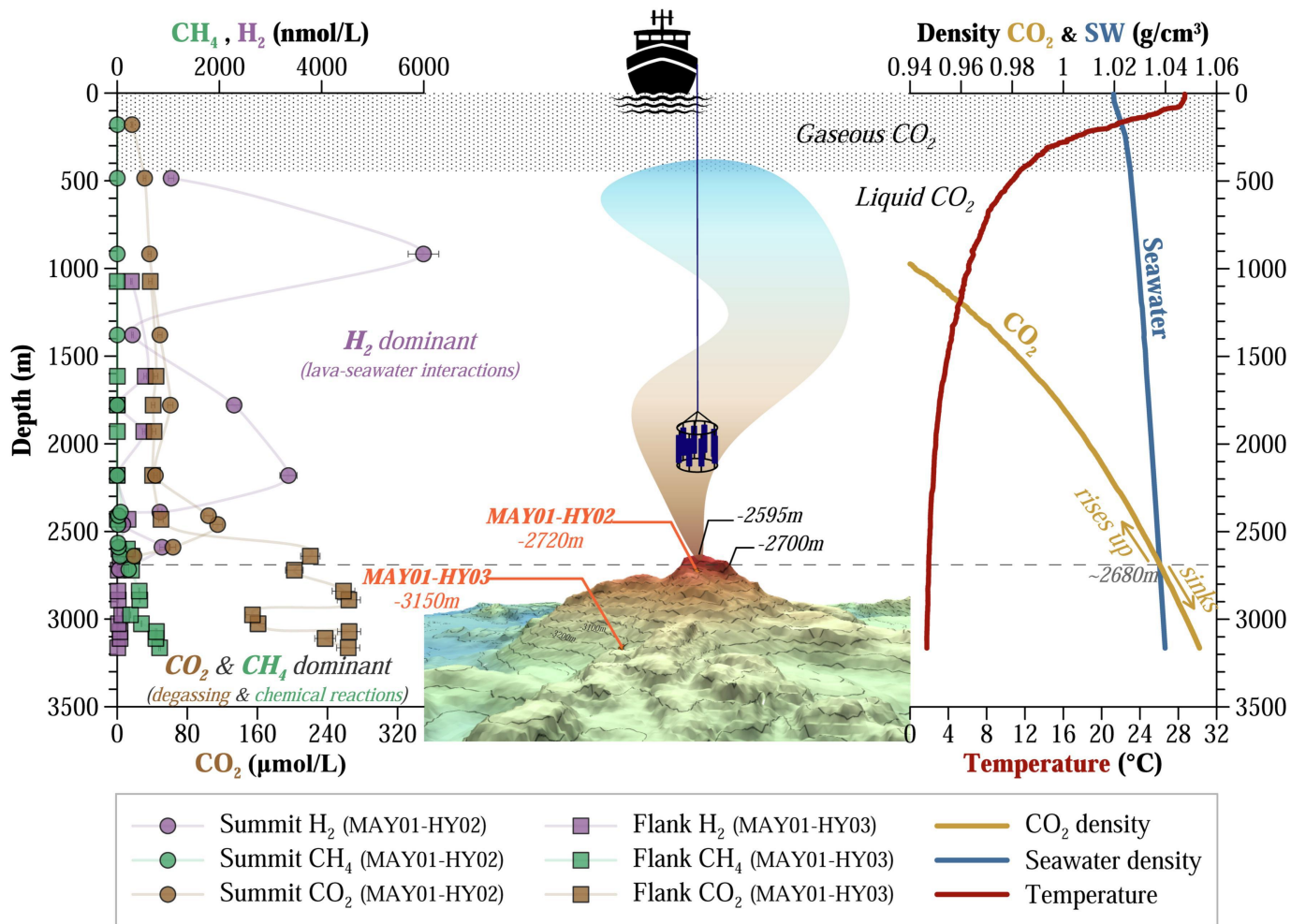


Figure 9

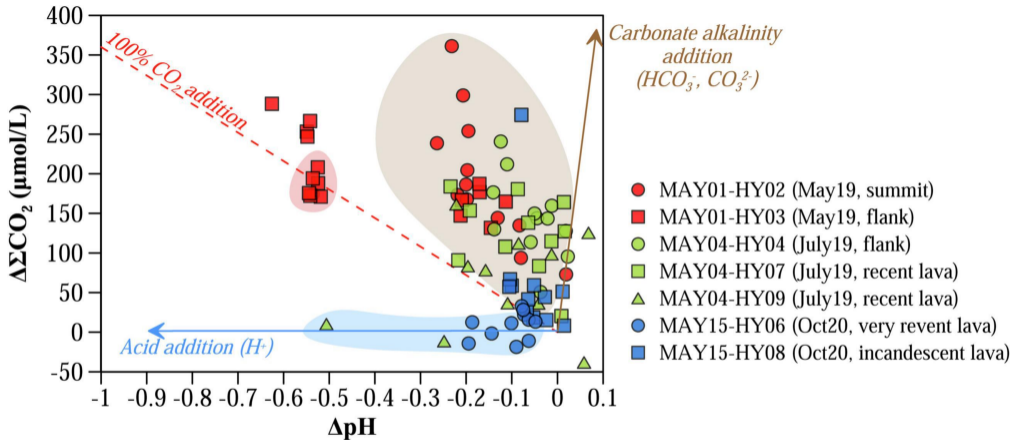


Figure 10